AN ABSTRACT OF THE THESIS OF

Thomas G. Shepard for the degree of Master of Science in Mechanical Engineering presented on December 9, 2005.

Title: Micro-bubble Dynamics in Two-Phase Flow Through a Micro-channel.

Abstract approved:

Redacted for Privacy

James A. Liburdy

An experimental investigation into the behavior of micro-bubbles flowing through a micro-channel has been conducted. Experiments were performed within a rectangular micro-channel with dimensions of 5 cm x 13.2 mm x ~130 μm. Bubbles were generated in an electrolyte solution by electrolysis at the lower channel wall near the inlet. A non-intrusive optical set-up utilizing laser induced fluoresce (LIF) from Rhodamine 6G and particle image velocimetry (PIV) seed particles was developed to obtain information on both phases of the flow using a single camera. The gas phase measurements are discussed here, while fluid phase data is discussed in a concurrent study. Measurements of bubble size, distribution, and area fraction were taken at four different heights above the lower channel wall for three different flow rates (40 mL/min, 80 mL/min, and 100 mL/min) and two different electrolysis voltages used to generate the bubbles. Digital images were processed with an involved, active algorithm intended to reduce noise. Bubble velocity measurements were obtained through a bubble pairing algorithm. It is determined that the use of electrolysis for bubble generation provides poor control of global area fractions while producing a non-homogenous bubble distribution across the channel width. Experimental results reveal that much noise remains after the digital image processing. Despite this, it is found that for measurements taken at the same channel position and local area fraction an increase in flow rate leads to an increase in mean separation distance of the bubbles. There is also evidence to suggest that under these conditions an increased flow rate causes small bubbles to disperse more quickly into the channel than large

bubbles. The bubble velocity results are shown to be very questionable by comparison with theoretical flow rates through the channel. Finally, a sensitivity analysis is done on the digital image processing technique used which reveals possible improvements that can be made to improve noise reducing capabilities.

Micro-bubble Dynamics in Two-Phase Flow Through a Micro-channel

by

Thomas G. Shepard

A THESIS

submitted to

Oregon State University

in partial fulfillment of
the requirements for the
degree of

Master of Science

Presented December 9, 2005

Commencement June 2006

Master of Science thesis of Thomas G. Shepard presented on December 9, 2005.

APPROVED:

Redacted for Privacy

Major Professor, representing Mechanical Engineering

Redacted for Privacy

Head of the Department of Mechanical Engineering

Redacted for Privacy

Dean of the Graduate School

I understand that my thesis will become part of the permanent collection of Oregon State University libraries. My signature below authorizes release of my thesis to any reader upon request.

Redacted for Privacy

Thomas G. Shepard, Author

ACKNOWLEDGEMENTS

I would like to acknowledge my advisor, Dr. James A. Liburdy, for all of the support, patience, and proficiency he provided throughout the undertaking of my research. I am also appreciative of Dr. Pence, Dr. Narayanan, and Dr. Gupta for serving on my committee. Additionally, a great many thanks are given to Dan Morse with whom this project was conducted. Finally I am obliged to my colleagues, both student and faculty, who enriched my experience at Oregon State with their insight, encouragement, and friendship.

TABLE OF CONTENTS

LIST OF FIGURES

LIST OF FIGURES (Continued)

Figure Page

LIST OF TABLES

LIST OF APPENDICES

LIST OF APPENDIX FIGURES

Nomenclature

A	Cross sectional channel area
A_{total}	Total area of frame
C	Pixel to micron conversion factor
D	Bubble diameter
$\overline{D}$	Average bubble diameter
Disp	Displacement of bubble
$\overline{Disp}$	Average bubble displacement
e	Pixel spacing of CCD array
F	Faraday number
h	Half channel height
I	Electric current
M	Molar weight
M_a	Total magnification of system
$\overline{MSD}$	Weighted average mean separation distance
MSD_{avg}	Mean separation distance in a single frame
msd	Minimum separation distance (distance to a bubble's closest neighbor)
n	Index of refraction
NA	Numerical aperture
P	Distance in pixels
P_{disp}	Bubble displacement in pixels
P_{msd}	Mean separation distance in pixels
Q_{O_2}	Rate of oxygen production
q	Volumetric flow rate
T	Laser pulse time lapse
t	Student t factor
u	Streamwise velocity
$\overline{Velocity}$	Average bubble velocity
Y	Distance measured from c channel centerline
y	Distance measured up from channel bottom
z	Number of electrons participating in reaction
δ_P	Pixel error
δ_C	Pixel to micron conversion error
δ_t	Laser pulse time lapse error
δz	Depth of field
λ	Wavelength
ρ_{O_2}	Oxygen gas density

INTRODUCTION

The use of micro-bubbles has been of great interest in many ubiquitous applications. Micro-bubbles are used for the enhancement of heat transfer in two-phase flows (Deng et al. 2003), for medical imaging through ultrasound techniques (Kevin et al. 1997) and are studied for better understanding of beer dispensing processes (Hepworth et al. 2004). In addition, they have been shown to successfully reduce skin friction up to 80% on flow over a flat plate when injected at the surface of the plate (Madavan et al. 1984).

The application of micro-bubbles as a drag reduction technique is quite appealing, especially when compared with some of the other technologies being explored for this purpose. While the use of riblets, large eddy break up devices (LEBUs), smart walls, and polymer injection have shown promise, the ease and potential for improved reductions make micro-bubble drag reduction the preponderant option. The frictional drag reduction is well suited to increase the efficiency of ships with large, flat hulls such as barges and cargo ships for which skin friction accounts for 80% of the total drag (Kodama et al. 2002). Furthermore, drag reduction improves with rougher surfaces, a desirable quality given the fouling of most ship hulls (Deutsch et al. 2003). Studies carried out by Kodama et al. (2002) on a 50 meter long flat plate have shown that a net drag reduction of 5% is obtained for fully loaded conditions.

Despite the number of past studies on the subject, further research is needed as the mechanisms of drag reduction are poorly understood. Knowledge of these mechanisms may lend itself to an optimization of efficient application of micro-bubble drag reduction. Also, the discrepant behaviors caused by the injection of micro-bubbles to flow through a channel have been found by Kato et al. (1999). The addition of micro-bubbles at low densities increased turbulent intensities but as bubble density increased, this result was reversed. This result demonstrates the complicated effect that micro-bubbles have on a flow and compels further experimental investigation into the dynamics of micro-bubble behavior. While many studies have

been carried out in large channels (~ millimeters deep) there has been little work done in micro-channels.

All of the antecedent applications of micro-bubbles require accurate measurement of micro-bubbles i.e. micro-bubble size, velocity, void fraction, spacing. Void fraction is defined as:

$$Void\ Fraction = \frac{Gas\ Volume}{Gas\ Volume + Liquid\ Volume} \tag{1}$$

One method for obtaining micro-bubble size, velocity, and local void fraction is the use of a fiber optic probe. However, this procedure is intrusive and unable to detect very small bubbles (Cartellier, 2001). Resistance measurements have also been used to measure void fractions (Cho et al., 2005), but this technique cannot determine characteristics of individual bubbles and is difficult to incorporate in experiments that use electrolysis as a means of bubble production. Recently an X-ray particle tracking technique was developed which allows for simultaneous measurement of the micro-bubble size and velocity in channels lacking optical access (Lee and Kim, 2005). While this method of data extraction is attractive, it utilizes an X-ray source which is not clinically safe, requiring special safety measures to be taken by users. Additionally, numerical simulations may be utilized to model micro-bubble two-phase flow. Nevertheless these studies are few, are limited by assumptions of bubble shape and velocity, and ultimately need to be verified by experimentation.

Advances in digital image processing have allowed for the creation of optical measurement techniques that permit simultaneous measurements of both the liquid and gas phases in two-phase flow. Particle image velocimetry (PIV) and particle tracking velocimetry (PTV), which involve the seeding of tracer particles into a flow, are two commonly used methods of flow visualization. These techniques frequently use fluorescent tracer particles that emit a Laser Induced Fluorescence (LIF) which passes through an optical filter before being recorded. During PIV and PTV image pairs are taken with a very short time lapse between the images; a computer algorithm is then applied to these image pairs to determine the velocity fields. Through careful selection of camera objectives, tracer particle size, and laser timing a wide range of

bubble size and velocity measurements is possible utilizing these methods. In order to obtain void fraction measurements from a two-dimensional digital image, assumptions must be made about bubble shape and bubble overlap. To avoid these assumptions the area fraction can be used and is defined as:

$$Area\ Fraction = \frac{Gas\ Area}{Gas\ Area + Liquid\ Area} \tag{2}$$

The focus of this work is aimed at two objectives. The first objective is to examine bubble dynamics in two-phase flow in a micro-channel. This involves the measurement of bubble size, bubble velocity, area fraction, and separation distances at different positions across a micro-channel and inspection of how these measurements change with different positions and different fluid flow rates. The second objective is to examine the ability of a PIV/LIF/PTV phase separating image processing technique to accurately measure both the liquid and gas phase of two-phase flow. This study is concerned with the gas-phase measurements while a concurrent study is investigating the liquid phase measurements.

LITERATURE REVIEW

Bubble behavior

Moriguchi and Kato (2002) studied the effect of injecting bubbles into flow through a channel which was 10 mm high, 100 mm wide, and 2000 mm long. The flow velocities ranged from 4-8 m/s while void fractions up to 0.15 were obtained by injecting compressed air through a porous plate at the upper surface of the channel. Bubble diameter was varied from 0.5 mm to 2.5 mm by using slightly different channel inlet geometries causing the flow velocity at the injection site to change. Digital images of the flow were taken and bubble diameters were determined using image processing software. It was found that skin friction on the upper surface of the channel decreased with increasing void fraction in agreement with earlier studies (Madavan et al., 1984) but the results differed by 10% compared to those obtained when using a channel with a height of 15 mm. It was further determined that as the average bubble diameter changed and void fraction remained the same there was very little change in the frictional resistance.

Kitigawa et al. (2003) studied bubble injection into flow through a vertical pipe with an internal diameter of 44 mm and a height of 1500 mm. Experiments were done with a bulk flow velocity of 176 mm/s and void fraction of 0.005 and 0.01. To examine the effect of bubble diameter at the same void fractions, a surfactant (3-Pentanol) was added to the fluid for one set of experiments. Adding surfactant caused the average bubble diameter to decrease from 2 mm for the no surfactant case to 1.1 mm. Measurements were taken using PIV/PTV and LIF techniques combined with a projection technique for bubble measurements. It was established that the distribution of void fraction across the channel depended on the average bubble diameter. Specifically, for the same global void fraction, the peak position of the void fraction distribution is closer to the channel wall for smaller bubbles. In another study reported in Kitigawa et al. (2003) it was found that changing bubble size had only a small effect on drag reduction which is in agreement with the findings of Moriguchi and Kato

(2002). The flow rates, channel dimensions, void fractions and bubble sizes were not given for this study.

Kawamura et al. (2004) investigated the effect of bubble size more closely. Their setup utilized a channel with a height of 120 mm and width of 50 mm. A flow velocity of 4 m/s was reported and 3-Pentanol was added to the flow to suppress bubble coalescence. A bubble-water mixture was injected at the upper surface of the channel and a commercial Computational Fluid Dynamics (CFD) code verified that the injected mixture did not cause separation or recirculation of the main flow. Two separate bubble generation techniques were used which produced average bubble diameters of 1.4 mm and 0.4 mm. An optical void fraction gauge determined local void fractions and photographs of bubbles taken from the side wall allowed qualitative assessment of the flow. It was determined that smaller bubbles disperse into the channel faster than the larger bubbles. This has little effect on drag reduction immediately downstream of the injection point, but as the flow progresses and the smaller bubbles continue to disperse away from the wall the drag reduction diminishes compared to the use of larger bubbles. It is concluded that the overall efficiency of drag reduction is decreased by dispersion for average bubble diameters of less than about .3 mm.

A numerical simulation of micro-bubbles seeded in a channel flow was done by Xu et al. (2002). The simulations used global void fractions of 0.04-0.08 at a nominal Reynolds number of 3000. Bubble diameters considered were 0.1h, 0.15h, and 0.3h where h is the half channel height. It is determined that the smaller bubbles are able to sustain drag reduction more effectively than the large bubbles. While this result differs from Kawamura (2004) the simulation finds void fraction distributions that agree with Kitigawa (2003).

Bubble measurement methods

As previously mentioned, PIV/LIF can be applied to two phase flow in a manner described by Sridhar et al. (1991). With this procedure, fluorescent tracer particles seed a flow and an optical long pass filter allows LIF to be recorded while filtering out laser light reflected by the bubbles. A second camera is needed to record images of the light that reflects off the bubbles. The weakness of this technique is that light reflected by the bubbles varies as the bubble changes position due to curvature effects. Also, any deformation by the bubble will change the position of reflection.

Another method for using PIV in two-phase flows permits separation of the phases using a digital masking technique (Gui and Merzkirch 1996). This technique does not separate the phases into two individual images on which PIV or PTV can be used, but is an operator in the PIV algorithm. The advantage of this process is that information on both phases is kept together and used in all recordings. The drawback with this method is that it assumes that each bubble is uniformly illuminated. Also, robust mask generation has proven difficult, implying that images with differing seed particle sizes, light intensities, noise, etc. require the formation of unique masks to match their conditions.

The Infrared Shadowgraphy Technique (IST) is a common method for measurements of bubbles. In IST a shadow image of the bubbles is recorded with a camera typically using an array of infrared light emitting diodes (LEDs) as a backlight to the flow or an infrared laser sheet in the flow and an optical filter. This causes the flow to be illuminated while bubbles are not, leaving a shadow of the bubbles in an image. Bubble velocities can be determined with a PTV algorithm. As IST can only capture bubble data, two separate cameras facing each other for IST and PIV are sometimes used to capture both phases (Kitigawa et al. 2003). Lindken and Merzkirch (1999) were able to use two cameras set at a 30^{o} angle to measure the flow velocity with two dimensional PIV and the bubble velocity with three dimensional PTV. The three dimensional bubble velocities were determined to be quite inaccurate due to faint bubble signals in the PIV measurements. Finally, a method has been developed that

allows both PIV and IST with a single camera (Lindken and Merzkirch 2002). This procedure captures digital images that include both tracer particles and bubble shadows in a single frame and has the advantage that the signals of each phase do not disturb each other in their respective PIV or PTV algorithms. Removal of interfering signal is accomplished through a digital image processing procedure which must be applied to every individual image.

Digital Image Processing

Due to the prevalence of digital imaging techniques in micro-bubble studies one finds a number of image processing algorithms for dealing with complications that arise. The problems that arise when trying to determine an appropriate algorithm for automatic bubble detection/labeling include laser speckle noise, reflected light noise, tracer particle removal, detection of in focus bubbles, and determination of overlapping bubbles. Surprisingly, much of the published work that adopts digital imaging processes neglects to include a description of how images are processed, which in this author's mind is relatively suspect due to the large impact processing can have on an image.

Honkanen and Saarenrinne (2002) recorded images of tracer particles and bubbles with the same camera and applied a median filter to separate the tracer particles out of the image while leaving just the bubbles. They note that the smallest bubbles were interpreted as tracer particles. After removing the tracer particles, bubbles were detected with a thresholding technique. The algorithm detected pixel segments that met an intensity threshold, area threshold, and a grey scale threshold.

Another example of a digital image processing algorithm is provided by Bröder and Sommerfeld (2002) who acquired IST images. Before a bubble detection algorithm could be applied a median filter was used to remove small scale noise. As a measure of bubble focus, an edge detecting Sobel filter was applied to determine the gradient of intensity values. A gradient threshold as well as a complete contour

(complete circumference) were used as detection criterion. Overlapping bubbles missing contour points were reconstructed using a cubic spline interpolation.

Dinh et al. (1999) captured backlit bubble images digitally and applied a multi-step bubble detection process. The first step was a preprocessing of the image to reduce noise and provide an improved background. Many filter possibilities are given for this step including minimum, maximum, averaging, and median filters, though a recommendation on when to use each is excluded. The second step is edge detection. It is determined that the Robert operator is the most susceptible to noise, the Sobel operator is more sensitive to diagonal edges than horizontal and vertical edges for which the Prewitt operator is more sensitive. Before performing edge detection the image was made binary with an intensity threshold. It is concluded that the automatically detected contours agree well with manually drawn contours.

A further example of digital image processing is given by Kitigawa et al. (2005) in a study that combined PIV, PTV, LIF, and IST. While the details are limited it is noted that image intensities are adjusted to emphasize bubble edges and to remove noise. An intensity threshold is determined from the histogram of pixel intensities in the image and used to binarize the image. They further state that binary labeling of bubbles allows for bubble deformation to be measured whereas a template matching method, which assumes a typical bubble shape, cannot. Correspondingly, binary labeling cannot separate overlapping bubbles while a template matching method can.

EXPERIMENTAL SET-UP

The test set-up was designed to obtain measurements of both the liquid and gas phases in micro-channel two-phase flow using a single camera. The primary components of the set-up include the micro-channel, optical set-up, and flow loop. A diagram of the entire set-up is shown in Figure 1.

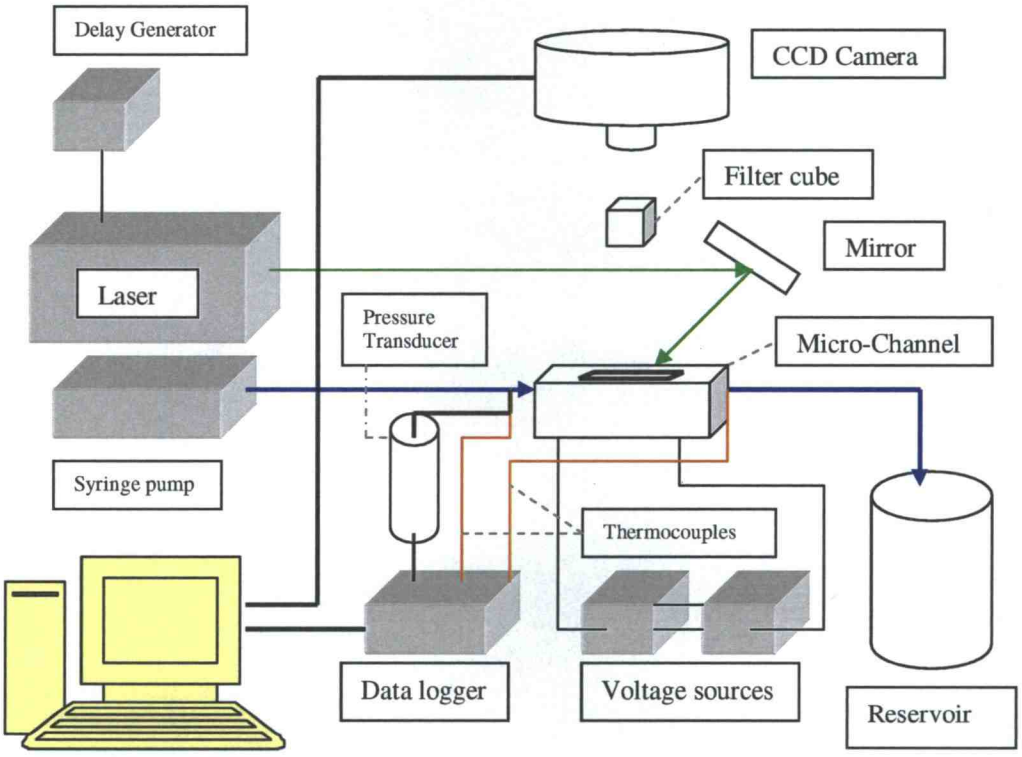

Figure 1. Schematic of experimental set-up

Micro-channel structure

The micro-channel is constructed used a layering technique in order to obtain micron order depths (Figure 2). The completed channel consisted of five layers: a base of Delrin Polymer, a Class VI medical rubber gasket with 0.005" thickness, a standard microscope glass slide with 1.1 mm thickness, a tempered spring steel shim

with 0.042" thickness and an aluminum compression plate. The inlet and outlet of the channel came up through holes drilled in the base layer and connected to barbed fittings with inner diameters of ~ 0.18". The channel base also had two 250 μm wide slots milled out in which electrolysis electrodes were placed. The electrodes were set below the lower channel wall, and the slots were milled near the inlet and outlet, so as to have minimal affect on flow characteristics. The overall micro-channel dimensions were 5 cm x 13.2 mm x ~130 μm.

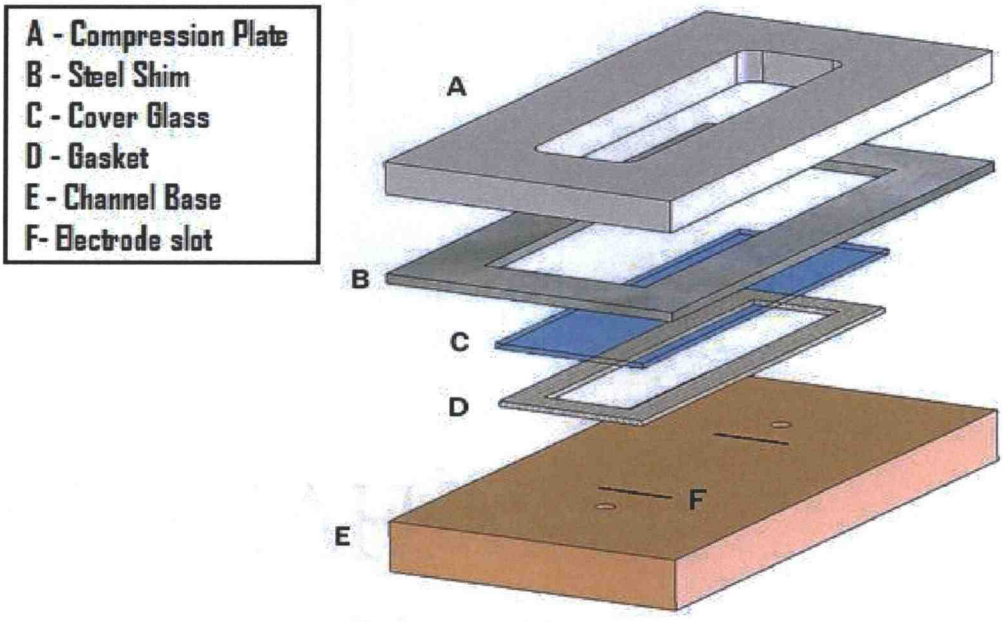

Figure 2. Micro-channel components. Used with permission of Dan Morse.

Optical set-up

The optical set-up is comprised of a laser, laser pulse timers, optical filter, and CCD camera. Laser light with a wavelength of 532 nm, from a Spectraphysics Quanta Ray Nd:YAG laser (Model PIV-400), was directed into the channel by a mirror. Light emitted and reflected from within the channel passes through a Nikon Wide Green Excitation G-2A epi-flourescent filter cube whose aim is to remove light with a wavelength below 590 nm from entering the camera objective. This filtering is

accomplished in a two step process. First, a dichromatic mirror reflects away light with wavelengths between 510-565 nm (Figure 3). In the second step a long pass emission filter removes light with wavelengths below 590 nm. While it may seem that this two-step filtering will prevent all light with a wavelength below 590 nm from reaching the camera, it must be noted that the cut-offs given do not prohibit 100% of light transmission at and below cut-off frequencies. A Mitutoyo M Plan Apo objective was used to magnify and focus the filtered light. This objective has a 10x magnification and a 0.28 numerical aperture. A Roper Scientific Micromax 1300 Y/HS CCD camera was used to capture optically filtered images of the flow. Images were taken with a resolution of 1300 x 1030 pixels. Synchronization of the laser and camera shutter was controlled by a Stanford Research Systems 4-Channel Digital Delay/Pulse Generator (Model DG535), allowing two images to be taken with a very small time (10-30 μs) elapsing between pictures. Captured images were recorded by a PC using Roper Scientific WinView32 version 2.5.5.1 software and saved for future processing.

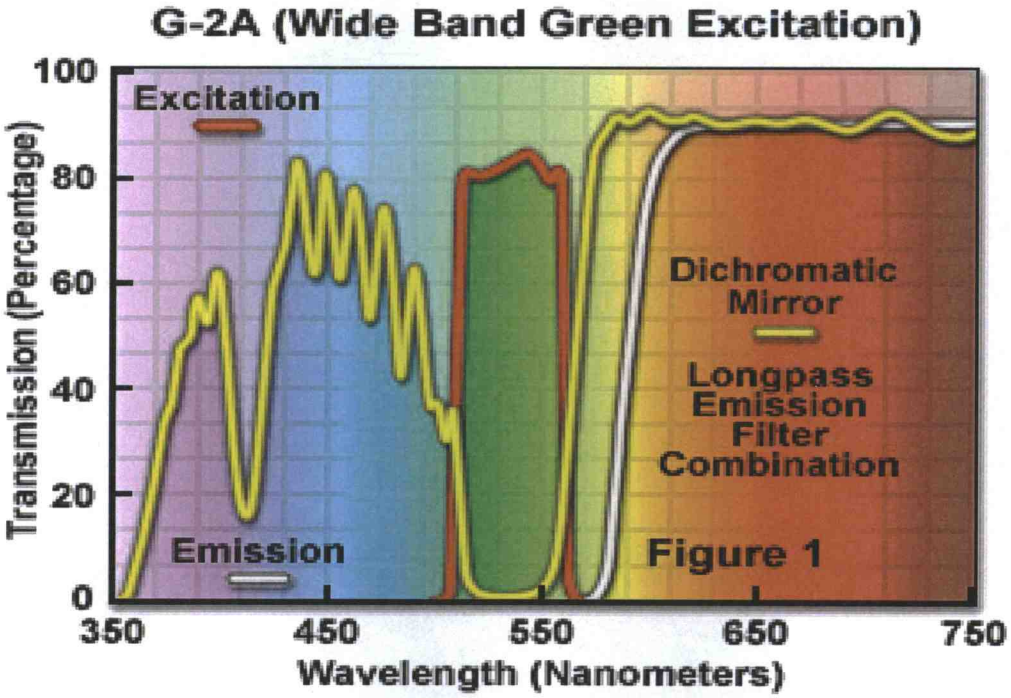

Figure 3. Optical filtering cube characteristics. Used with permission from Nikon website.

The area of investigation for this set-up depends on the depth of field (δz) of the optical system and on the camera height above the channel. Determination of the depth of field for the optical set-up takes into account many factors and is described by Meinhart et al. (1999):

$$\delta z = \frac{n\lambda}{NA^2} + \frac{ne}{M_a NA} \tag{3}$$

From this, the depth of field is calculated to be approximately 11 μm. Camera position above the channel is controlled by mounting the camera to a vertical traversing mechanism (Parker Positioning Systems) which allowed vertical position to be determined within 1 μm.

Flow additives

Owing to the use of PIV and electrolysis, flow additives were introduced to the liquid solution. For effective electrolysis an electrolyte solution was required. To this end, 3 percent (by weight) de-ionized salt (NaCl) was mixed with de-ionized water. For the concurrent PIV study, tracer particles were added to the flow. A solution of Duke Scientific Red-Fluorescing Polymer Microspheres (Model R200), which had beads with a diameter of 2 μm and density 2.4 x10^9 beads/mL, was mixed with the electrolyte solution at a rate of 10 drops per 100 mL. These microspheres have a maximum emission at 612 nm allowing their emitted light to pass through the optical filter. Rhodamine 6G (Molecular Probes, Model R-634) was also added to make a 1.8 x10^{-4} molar solution. This substance is a fluorescing dye that has a maximum absorption at about 528 nm and a maximum emission of about 551 nm. The reason for including Rhodamine 6G was to produce LIF from all liquid components of the channel flow. Dye concentration was chosen so that the seed particle emission would be intense enough to stand out from that of the dye when filtered with the technique

described above. Yet bubbles in the flow ideally should not fluoresce, meaning that bubbles will appear darker in the captured images except in the case that reflected light is intense enough to survive attenuation by the filter and be recorded by the camera.

As seen in Figure 4, the optical set-up and flow additives effectively create black interiors for bubbles that are larger in size. Smaller bubbles do no show this effect, most likely due to the reflection of the intense laser light and/or focusing of light emitted by the dye. An additional explanation conjectured by Kitigawa et al. (2003) is that fluorescent materials may collect at a bubble surface due because of its electro-chemical properties. Figure 4 also shows the seed particles as small bright spots that stand out from the gray background create by emission from the dye. The fact that dye emission survives through the filters is due to its spectral emissive characteristics. While Rhodamine 6G has a peak emissivity at 560 nm, corresponding to a normalized emission strength of 1, it is shown to have a normalized emission strength of 0.3 at 600 nm (Sage et al. 2001). For this reason, a substantial amount of light emitted by the dye remains after filtering.

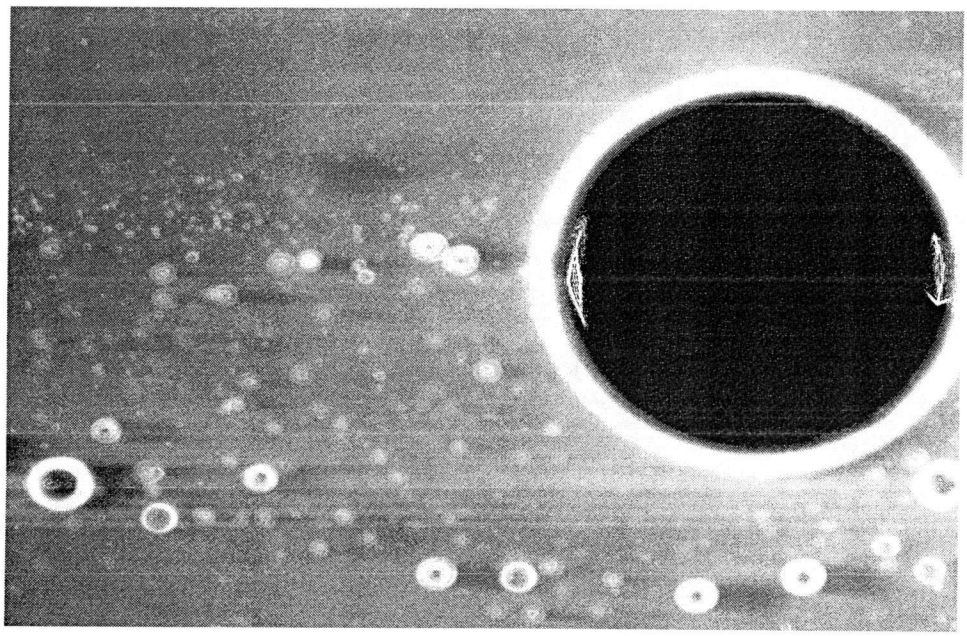

Figure 4. Bubble image displaying bubble, dye, and seed particle intensities

Flow loop

Fluid flow (labeled with blue arrows in Figure 1) through the channel was produced with the use of Cole Parmer 74900 series syringe pump. By varying the pump speed and the number of syringes used, flow rate through the channel was varied. After passing through the micro-channel, flow was collected in a reservoir from which the fluid was typically reloaded into the syringes for another run through the channel.

To monitor channel pressure and fluid temperature a pressure transducer and a pair of thermocouples were incorporated. At the micro-channel inlet an Ashcroft Drebber Industries pressure transducer (Model K17M0215F260) and thermocouple monitored conditions while at the outlet another thermocouple monitored outlet temperatures. The reasoning for measuring both inlet and outlet temperatures was to determine the effect that electrolysis had on fluid temperature in the channel. The transducer and thermocouples were connected to Fluke Hydra series data logger and its corresponding software was used to save data to a PC for future processing.

Electrolysis

As previously mentioned, the method of micro-bubble generation is electrolysis. When a voltage is applied between the negative anode (upstream electrode) and the positive cathode (downstream electrode) a current of charged ions flows through the channel. At the anode, oxygen gas forms by the electrochemical reaction (Wedin et al., 2003):

$$2H_2O \rightarrow 4H^+ + 2e^- + O_2 \tag{4}$$

As the oxygen gas forms at the anode it is carried away in the form of bubbles by the fluid flowing through the channel. From Faraday's law the rate of oxygen production is calculated as:

$$Q_{O_2} = \frac{IM}{zF\rho_{O_2}} \tag{5}$$

In an experiment by Wedin et al. 2003 it was demonstrated that the accuracy with which Faraday's law predicts gas production is questionable. In the current study the electrodes used were platinum wires with a diameter of 75 μm. The voltage applied across the electrodes was supplied by two Agilent DC voltage sources (Model E3617A).

Test conditions

With this experimental set-up multiple flow conditions were available for measurement. Test conditions are listed in Table 1 where shear is calculated based on a channel height of 130 μm. Three flow rates were used in the current study: 40 mL/min, 80 mL/min and 100 mL/min. Higher flow rates could not be tested as the syringe pump failed to operate reliably above 100 mL/min. As a way to vary global area fractions, the electrolysis voltage was varied. At 40 mL/min, a voltage of 60 V and 90 V was used while at the higher flow rates 90 V and 120 V were applied. By traversing the camera vertically images could be captured at differing channel heights. The channel heights used were y/h = 0.1, 0.3, 0.5, 1. Images were captured from an area roughly midway between the electrolysis electrodes and midway between the side walls. A total of 24 (4 heights x 3 flow rates x 2 voltages) different tests with bubbles were run and 12 tests without bubbles (0 voltage) were run. Roughly 40 image pairs were taken for each test making the total number of images processed nearly 2000.

Table 1. Experimental test conditions

Measurement Position (y/h)	Flow Rate (mL/min)	Electrolysis Voltage (V)	Local Shear Rate (1/s)
0.1	40	0, 65, 90	-3227.5
	80	0, 90, 120	-6455
	100	0, 90, 120	-8068.9
0.3	40	0, 65, 90	-2510.3
	80	0, 90, 120	-5020.6
	100	0, 90, 120	-6275.8
0.5	40	0, 65, 90	-1793.1
	80	0, 90, 120	-3586.2
	100	0, 90, 120	-4482.7
1	40	0, 65, 90	0
	80	0, 90, 120	0
	100	0, 90, 120	0

PROCEDURE AND DATA PROCESSING

Channel height determination

Before running a test, the exact channel height was determined. This was done so that the camera height could be accurately adjusted to take measurements at a desired channel height. To determine the channel height, the camera was focused on the top and bottom channel wall, and camera position at each location was recorded. The top of the channel was found by focusing on a few small scratches put on the lower surface of the microscope slide which provided the upper wall of the channel. When the top of the channel was located its exact position was determined with the following process. One student would adjust the camera height slowly so that the focal plane was just below the upper channel wall. As the focal plane was slowly moved towards the upper channel wall another student monitored the images continually taken by the camera, paying close attention to the focus of discernible features in the image. When this student felt that the image was in focus the height of the camera was recorded by the student in charge of adjusting its height. The process of moving the focal plane below the upper channel surface and bringing it back up until the image was deemed in focus was repeated a total of seven times. These seven measurements were averaged to determine the average upper channel bottom focus height. Next, the focal plane was adjusted so that it was above the upper channel wall and then slowly lowered back towards the upper channel wall until the second student deemed the image to be in focus. The camera height was again recorded and the process was repeated for a total of seven measurements allowing for an average upper channel top focus height to be determined. The upper channel height was then determined as the mean of the average upper channel top and bottom focus heights. This procedure was then repeated for the lower channel wall. To ensure that the channel and/or camera did not move during a run the process of finding the lower channel wall height was repeated after a test. A comparison of pre and post-test lower

channel heights typically showed a movement of ~ 1-2 μm which was considered negligible.

Table 2. Measured channel heights

Flow Rate (mL/min)	Measurement Positions (y/h)	Electrolysis Voltage (V)	Channel Height (μm)
40	0.05	0, 65, 90	107
	0.15	0, 65, 90	125
	0.25	0, 65, 90	131
	0.5	0, 65, 90	131
80	0.05	0, 90, 120	107
	0.15	0, 90, 120	125
	0.25	0, 90, 120	131
	0.5	0, 90, 120	131
100	0.05	0	103
		90, 120	138
	0.15	0	138
		90, 120	137
	0.25	0, 90, 120	137
	0.5	0	143
		90, 120	139

Image Processing Algorithm

Images captured during a test were saved as a single file with two image frames. These files were split with MatLab (version 7.0.1) to produce two single files with a single frame each. A flowchart of the image processing algorithm developed with MatLab is shown in Figure 5.

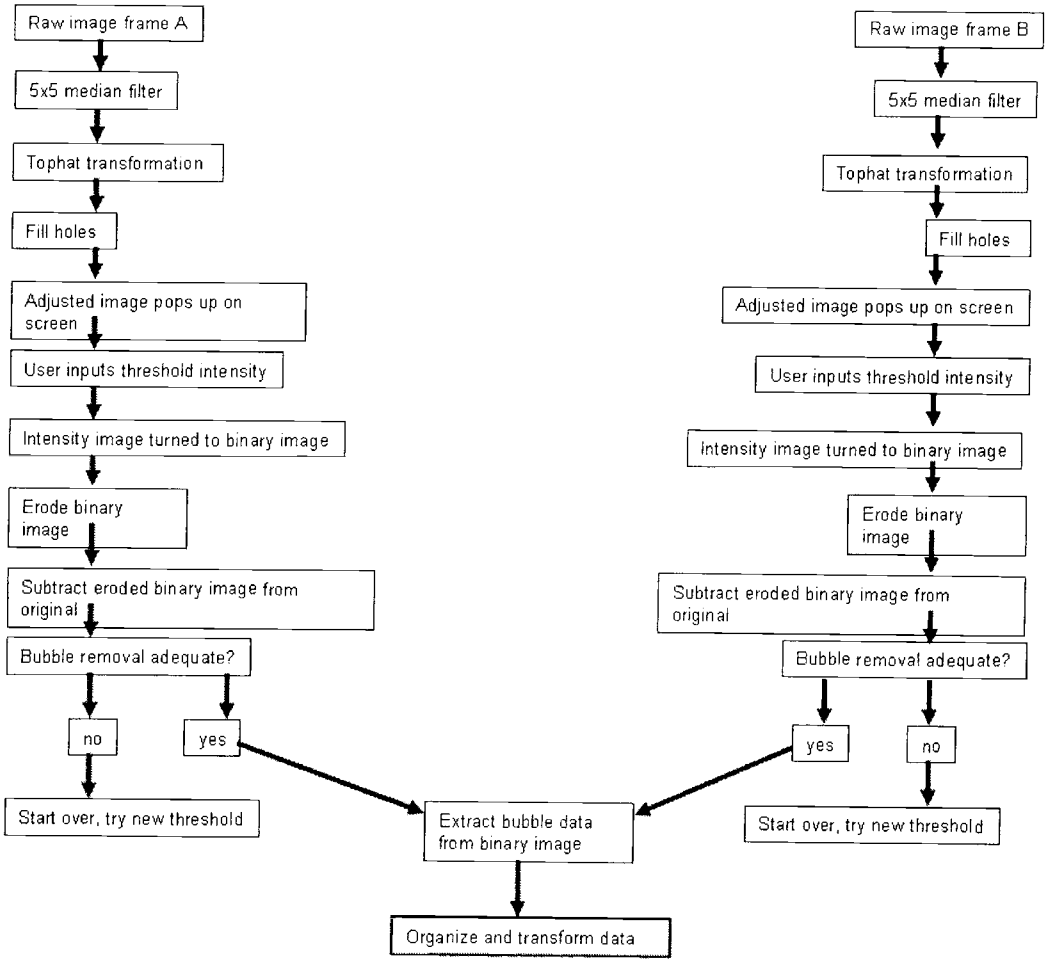

Figure 5. Digital image processing flowchart

In order to isolate the bubbles in the original image (Figure 6) a 5 x 5 median filter (medfilt2) was applied to reduce tracer particle intensities and even out noise (Figure 7). Next a tophat transformation (imtophat) was used to create a more uniform background (Figure 8). In this transformation the convolution element used was a 55 pixel radius disk. The size of this element was chosen so that it would be larger than most bubbles in an image. It was found that due to reflective properties, bubble circumferences were often illuminated above the background intensity. The fill holes command (imfill) was used to fill in all bubbles that displayed a distinct circumference with intensity above the background intensity (Figure 9). Comparing Figure 8 and

Figure 9, it is seen that the intensity of bubble interiors is increased in Figure 9. Then a binarization intensity threshold was iteratively, and actively, determined. In this procedure the semi-processed image was monitored by the author. The intensity of noise was compared with that of bubbles and an intensity threshold was chosen. If an image was excessively noisy it was removed from the data set, see Appendix A. About 5% of image pairs were removed due to excessive noise. The decision to actively determine an intensity threshold was due to the fact that laser power and noise levels varied from image to image making it difficult to implement an automatic threshold algorithm with a robustness to accommodate the changing conditions. Utilizing the actively determined intensity threshold the image was made binary (im2bw) as shown in Figure 10. In this step MatLab labels each bubble as an object for which measurements can automatically be made. Next, the image is eroded (imerode) with a convolution element comprised of a 2 pixel radius disk (Figure 11). This step shrinks the bubbles slightly to reduce the halo effect and decreases salt noise that was binarized as is seen by comparing Figure 10 and Figure 11. The eroded picture is then subtracted from the original and viewed (Figure 12). Subtraction of the eroded image allows the degree of bubble identification to be easily seen. Furthermore, this step was used to remove bubbles from images but leave seed particles so that PIV could be done in the concurrent study. At this point in processing a judgment of bubble identification is made. If the picture shows that significant noise is being identified as bubbles, or that many bubbles have been left out, an iterative method of threshold determination is begun. A new intensity threshold is determined based on information gained about the degree of noise that survives or bubbles that are left out. The new image is then eroded and subtracted from the original. When the bubble removal/identification is deemed adequate the entire image processing algorithm is performed on the second image of the image pair.

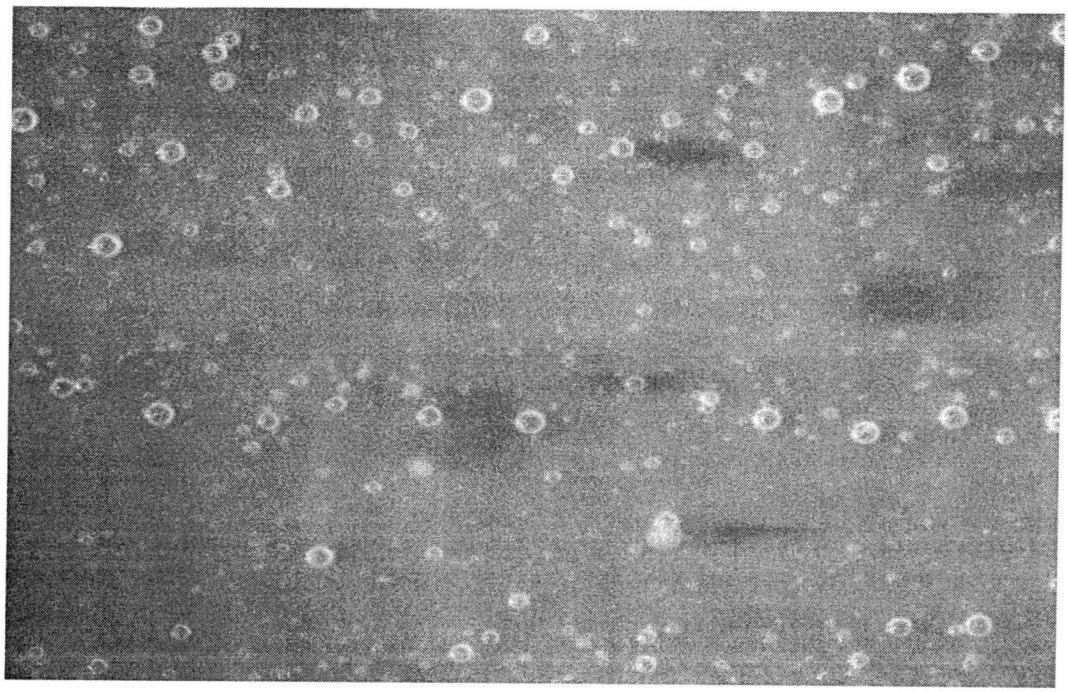

Figure 6. Original image

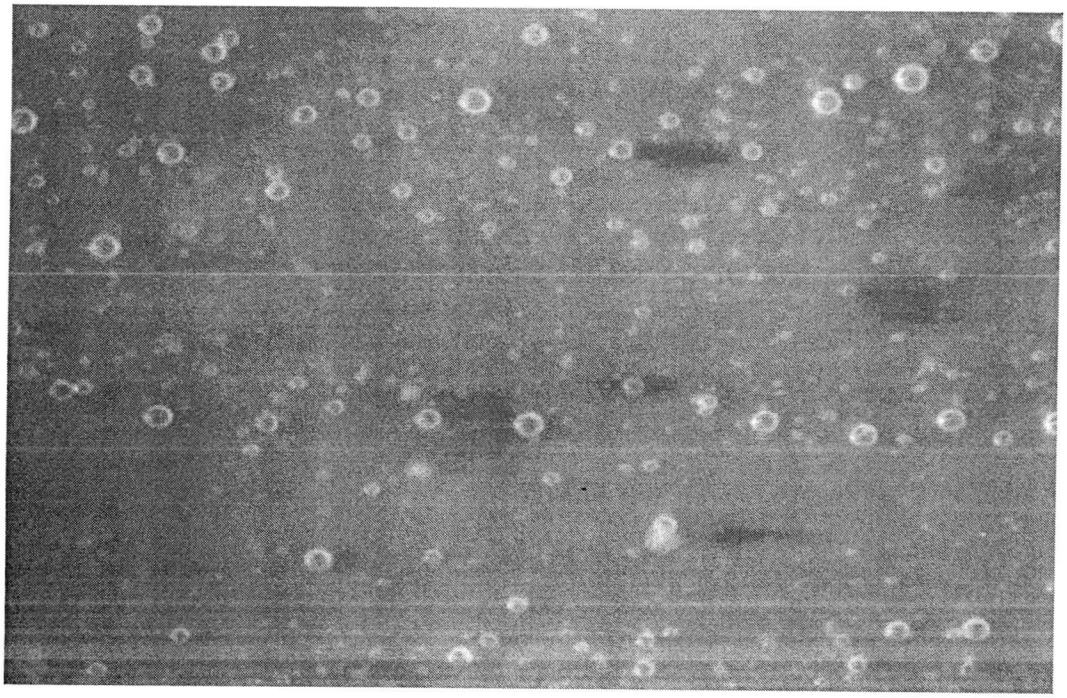

Figure 7. Median filtered image

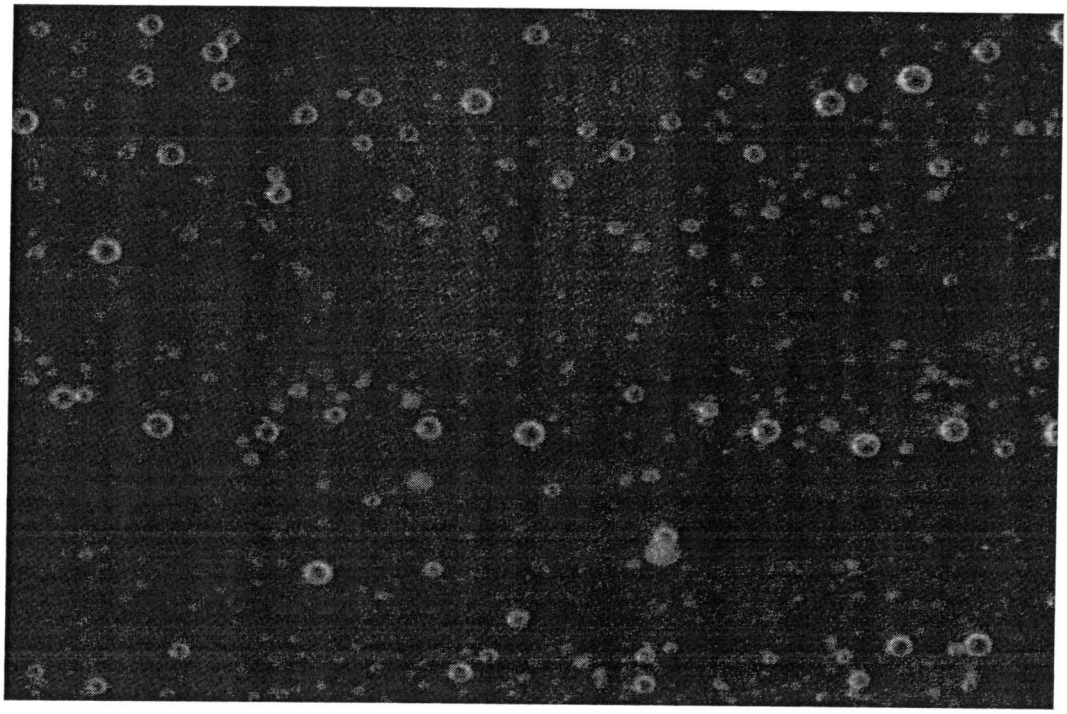

Figure 8. Tophat transformed image

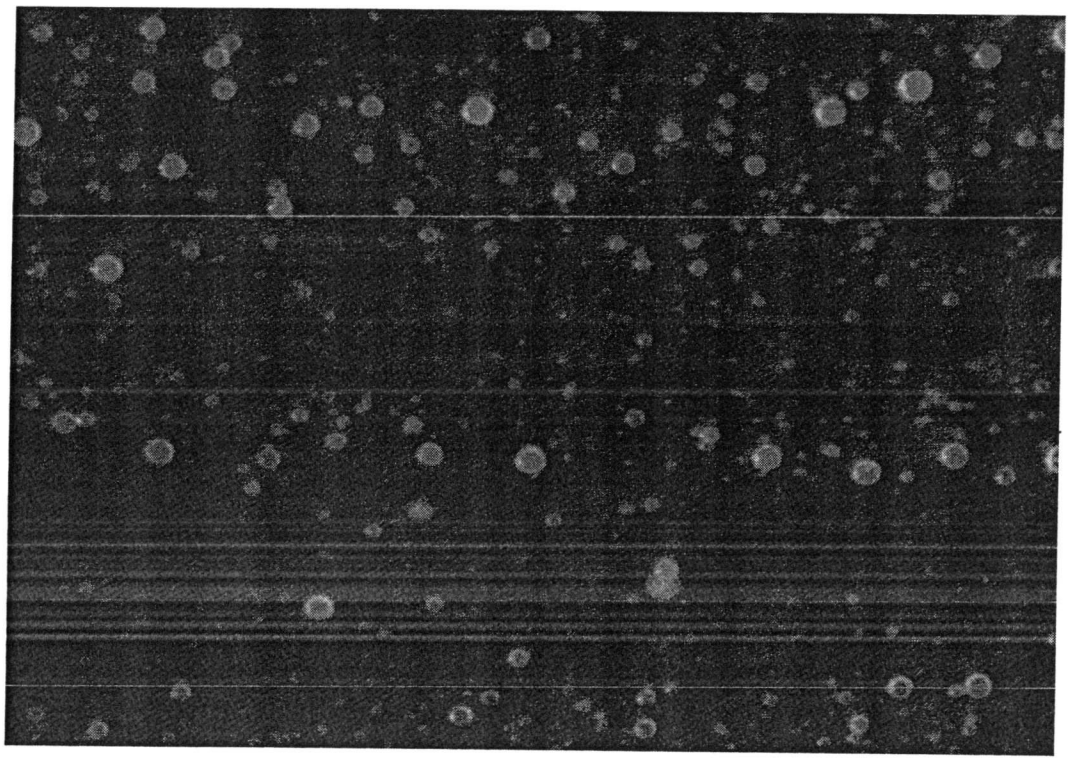

Figure 9. Image after holes are filled

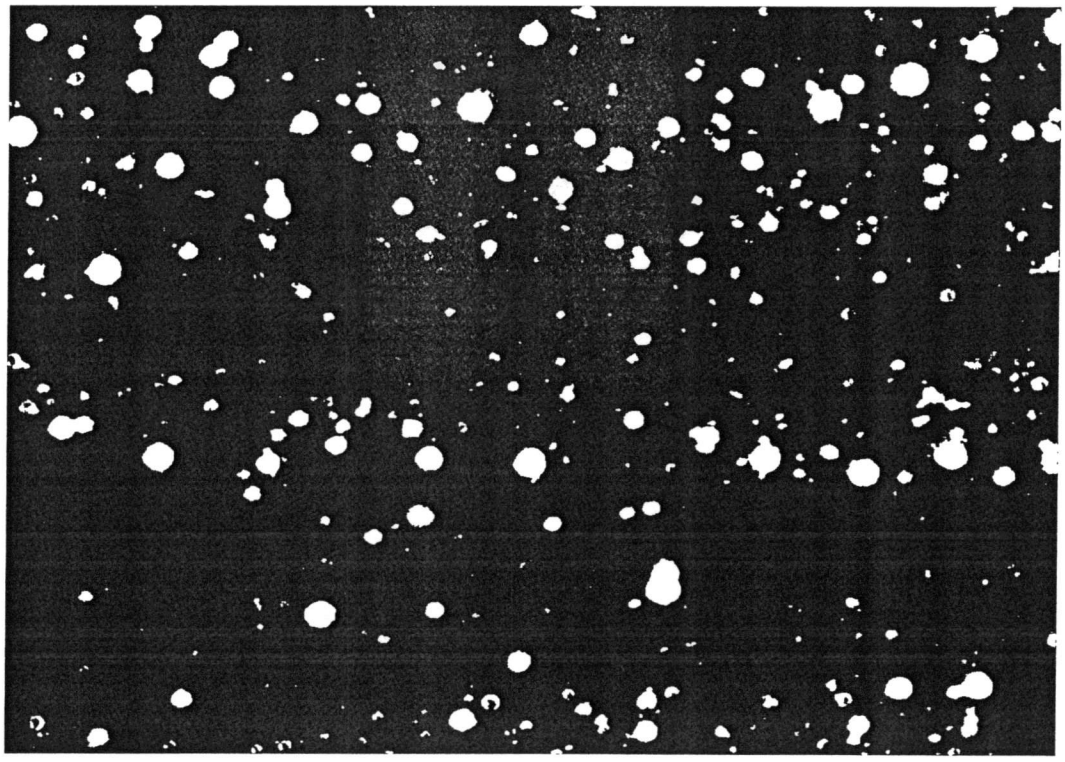

Figure 10. Binary image

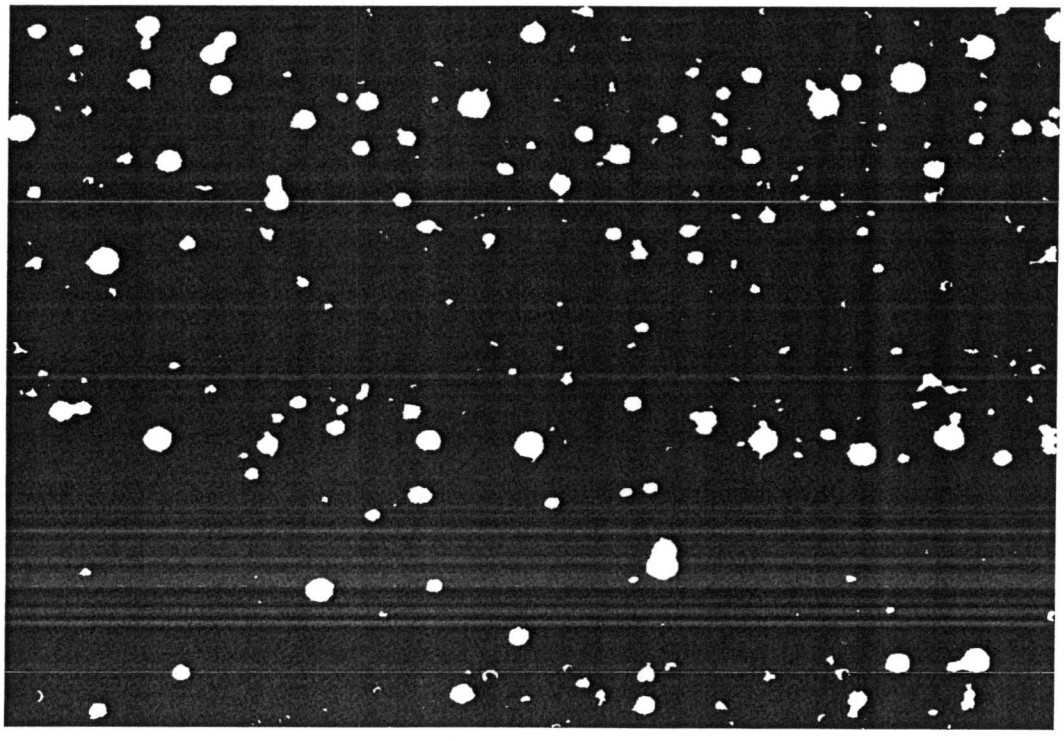

Figure 11. Eroded binary image

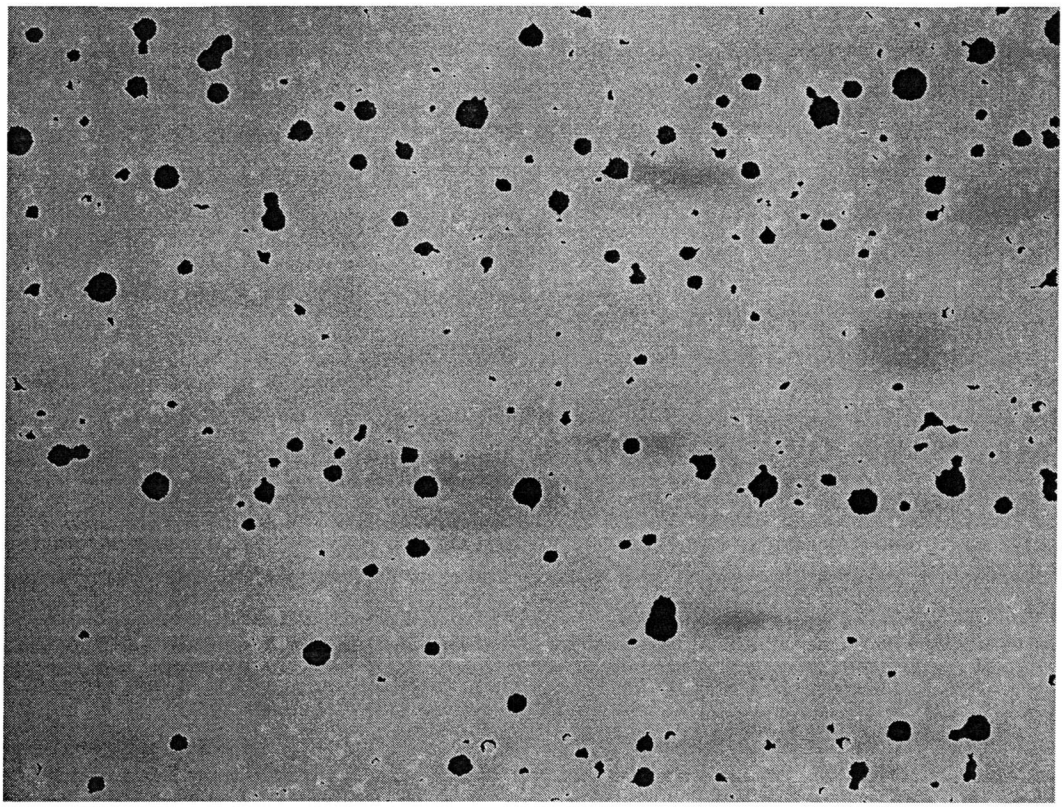

Figure 12. Eroded image subtracted from original image

From the binary images MatLab determines the equivalent bubble diameter, eccentricity, and centroid for each bubble in a frame. Information on every bubble in every frame for a run is stored for later processing. The data processing procedure extracts information on mean separation distances, number of bubbles, and area fraction in a single frame. Mean separation distance refers to the average distance from any bubble's centroid to its closest neighbor's centroid. Mean separation distances are determined for the 1^{st}-5^{th} closest neighbor in an image. Also, in the data processing procedure bubbles in both frames of an image pair are paired up according to an algorithm explained in Appendix B.

Theoretical flow calculation

To gain insight into velocity results that are obtained for the bubbles, the theoretical velocity distribution in the channel is calculated:

$$u = \frac{3}{2}\frac{q}{A}\left[1-\left(\frac{Y}{h}\right)^2\right] \tag{6}$$

Derivation of this relation assumes steady 2-dimensional flow with negligible gravity forces through a channel with parallel, fixed walls. The first three of these assumptions are assumed to hold reasonably well in the current study as measurements are taken midway across the channel where side wall effects are diminished, gravity forces will be insignificant for a ~ 130 μm change in elevation, and the syringe pump specifications show it to be quite accurate (± 0.5% with ± 0.2% reproducibility). With this formula fluid velocities can be obtained at different channel heights for theoretical flow through the micro-channel without bubbles.

RESULTS AND DISCUSSION

In this section results from the digital image processing sensitivity analysis and data analysis are presented and discussed. Excluding data presented in the digital image processing sensitivity analysis, the results given are averaged values incorporating data from all processed image pairs for a test. Every bubble diameter from all image frames in a test was compiled together before being averaged. Area fractions and bubble velocities were averaged in this way also. Mean separation distances are averaged using a weighted average scheme (see Appendix C). For each image, a mean separation distance is calculated by averaging the distances from each bubble to its closest neighbor. The use of a weighted average allows a mean of the mean separation distances to be computed using the uncertainties for each as a weight.

Digital Image Processing Sensitivity

When different filters and transformations are applied during digital image processing, measurements made within the image are altered. This subject is one which receives little to no mention in available literature. In the current study a median filter, tophat transformation, and erosion were applied to every image and each of these involved the definition of a convolution window shape and size. In an effort to exhibit the sensitivity of measured quantities on these criteria, five random image pairs were processed with varying convolution window sizes. Disk 1 refers to the convolution window used for the tophat transformation; Disk 2 is used in the erosion step. For each frame the number of bubbles, area fraction, bubble diameters, and mean separation distances for a bubble's five closest neighbors (Sep. Dist. 1, Sep. Dist. 2, etc.) were recorded. The plotted data (Figure 13-24) show the area fraction averaged over both frames in an image pair, the average bubble diameter of all bubbles in both frames, the number of bubbles in frames A and B and the mean separation distance to a bubble's closest neighbor averaged over both frames.

Figures 13-15 show how average bubble diameter changes with differing filter sizes. It is interesting the note that the average bubble diameter does not show a

significant trend when the size of Disk1 or Disk 2 (erosion) is changed. One can imagine that as Disk 2 gets larger more noise is removed from a processed image, reducing the number of small "bubbles" which would lead to an increased average diameter. At the same time though, the bubbles that remain shrink slightly which would lead to a decreased average diameter. Seemingly these two effects roughly balance each other out. Examination of Figure 15 reveals a slight increase of average bubble diameter with larger median filters suggesting that an increased median filter may reduce noise.

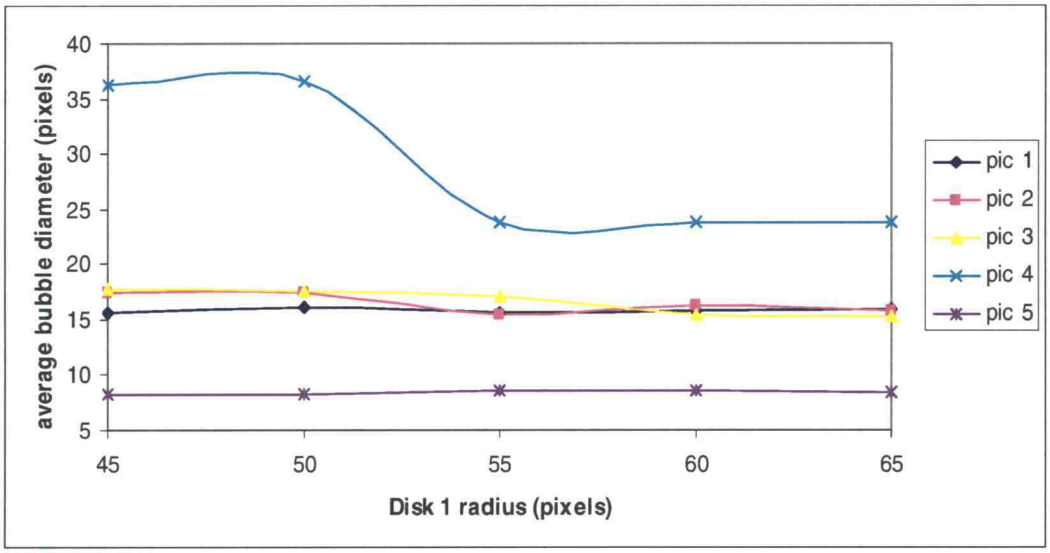

Figure 13. Sensitivity of average bubble diameter to Disk 1 size

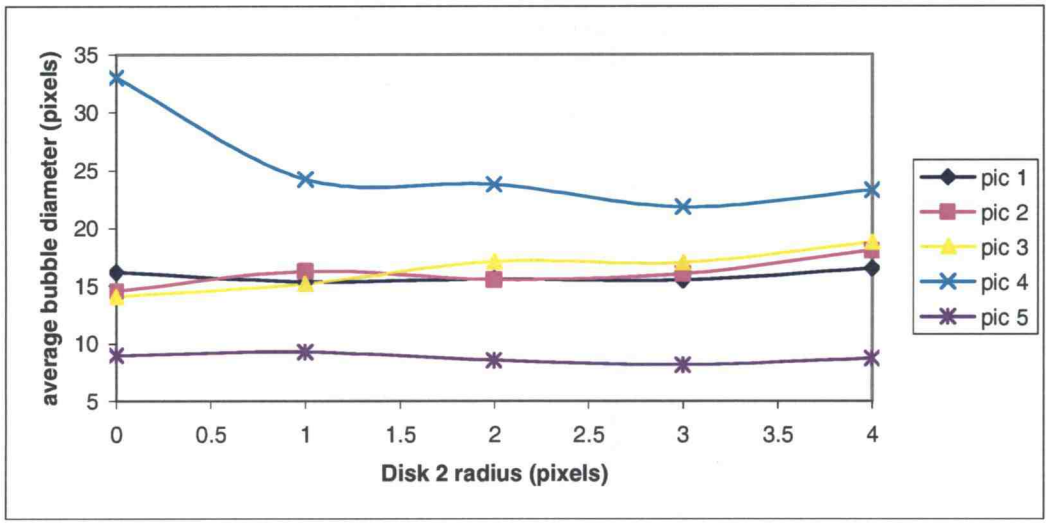

Figure 14. Sensitivity of average bubble diameter to Disk 2 size

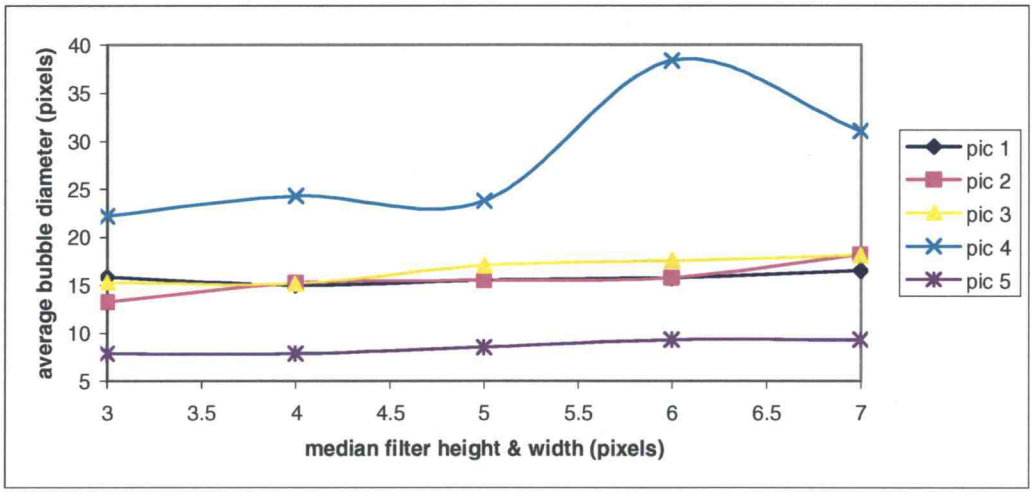

Figure 15. Sensitivity of average bubble diameter to median filter size

The dependence of area fraction on filter sizes is seen in Figures 16-18. As expected area fraction decreases with increasing Disk 2, while it increases for increasing Disk 1. As these two trends oppose each other it is difficult to say with any certainty that any given filter size is more appropriate than another in terms of effect on area fraction. Also, Figure 18 shows a small decrease in average area fraction with increasing median filter size. Recalling that average bubble diameter increased for

larger median filters, this provides further substantiation that an enlarged median filter reduces noise.

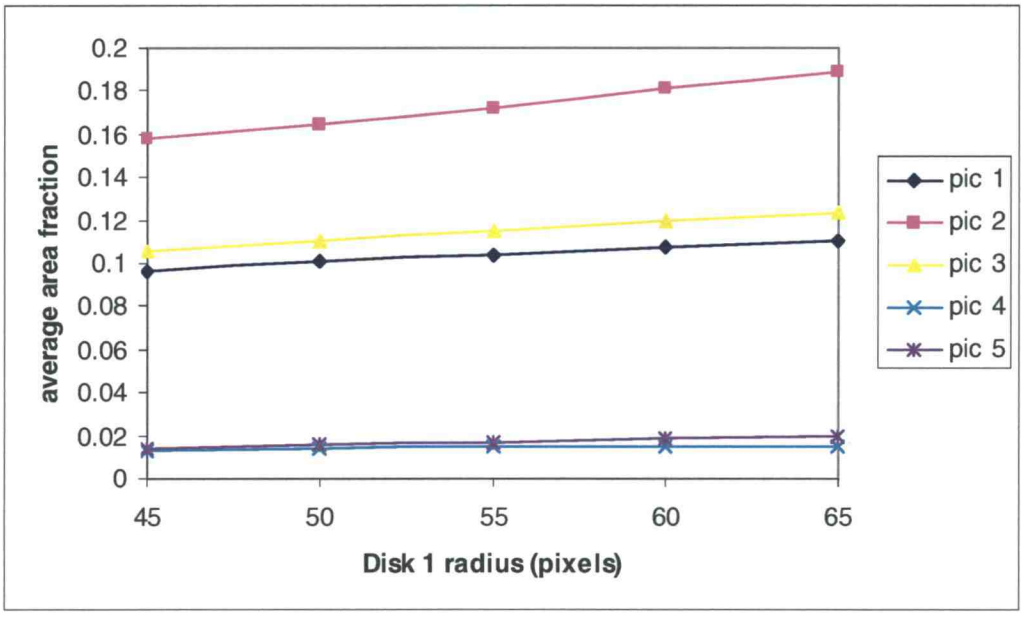

Figure 16. Sensitivity of average area fraction to Disk 1 size

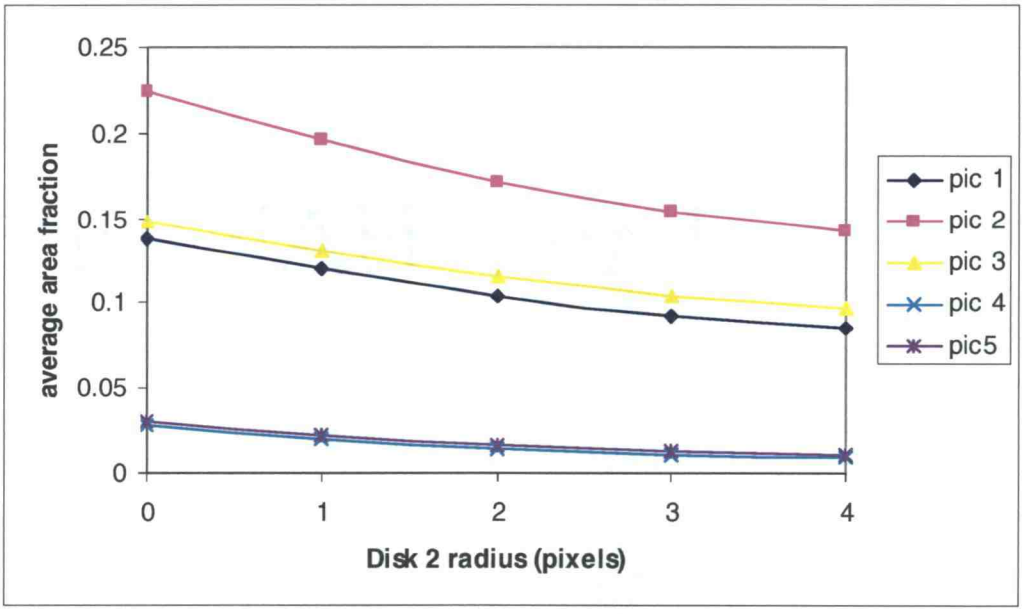

Figure 17. Sensitivity of average area fraction to Disk 2 size

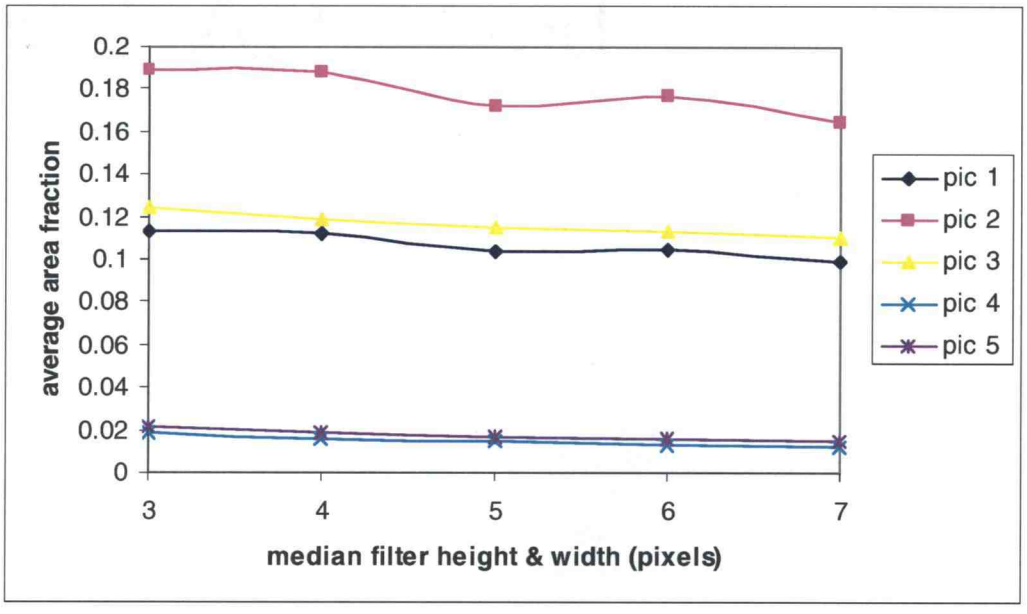

Figure 18. Sensitivity of average area fraction to median filter size

The number of bubbles in an image is strongly affected by the choice of filter size as is apparent in Figures 19-21. Increasing Disk 1 is shown to slightly increase the number of bubbles, implying that more noise is present due to a less complete evening out of the background. The strong decrease in number of bubbles with an increasing Disk 2 suggests that a larger erosion element may significantly reduce noise that remains in a binary image. What is not clear though is whether or not small bubbles would be eradicated also with an increased Disk 2. A reduction in noise levels also appears possible by using a larger median filter (Figure 21). In addition to information of noise levels obtained from these plots, one may note the consistency with which the digital image processing technique employed labeled bubbles from frame to frame. This is shown in the qualitative and quantitative similarities between the number of bubbles detected for both frames of an image pair.

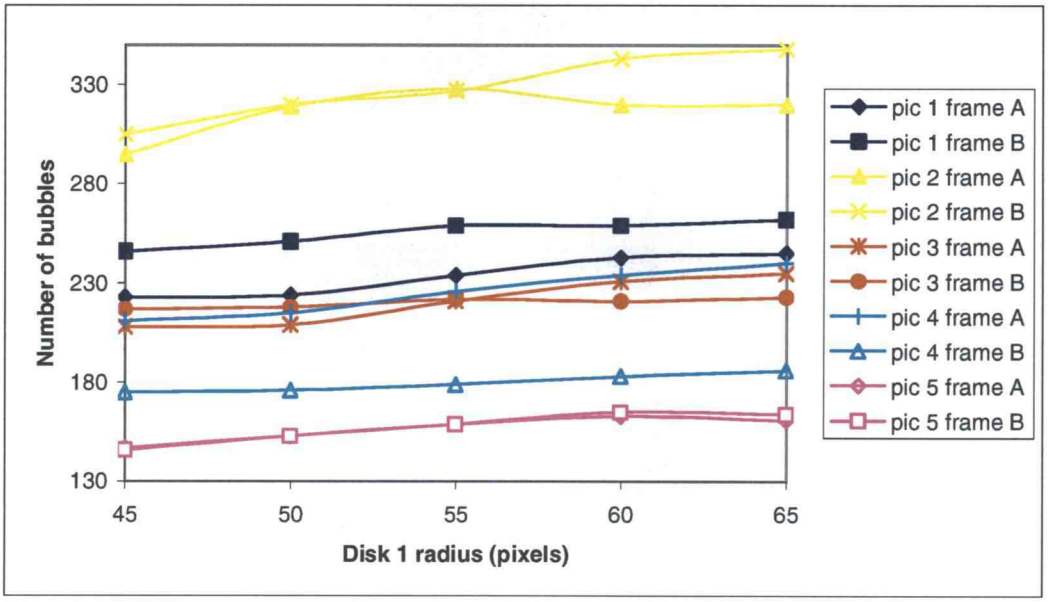

Figure 19. Sensitivity of number of bubbles to Disk 1 size

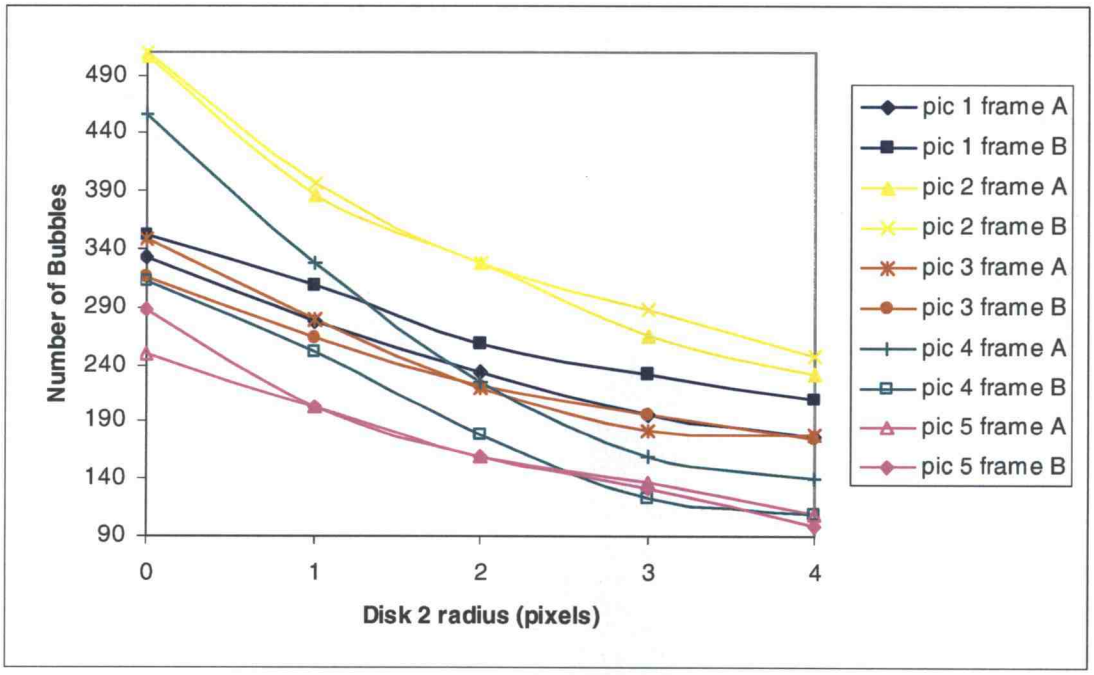

Figure 20. Sensitivity of number of bubbles to Disk 2 size

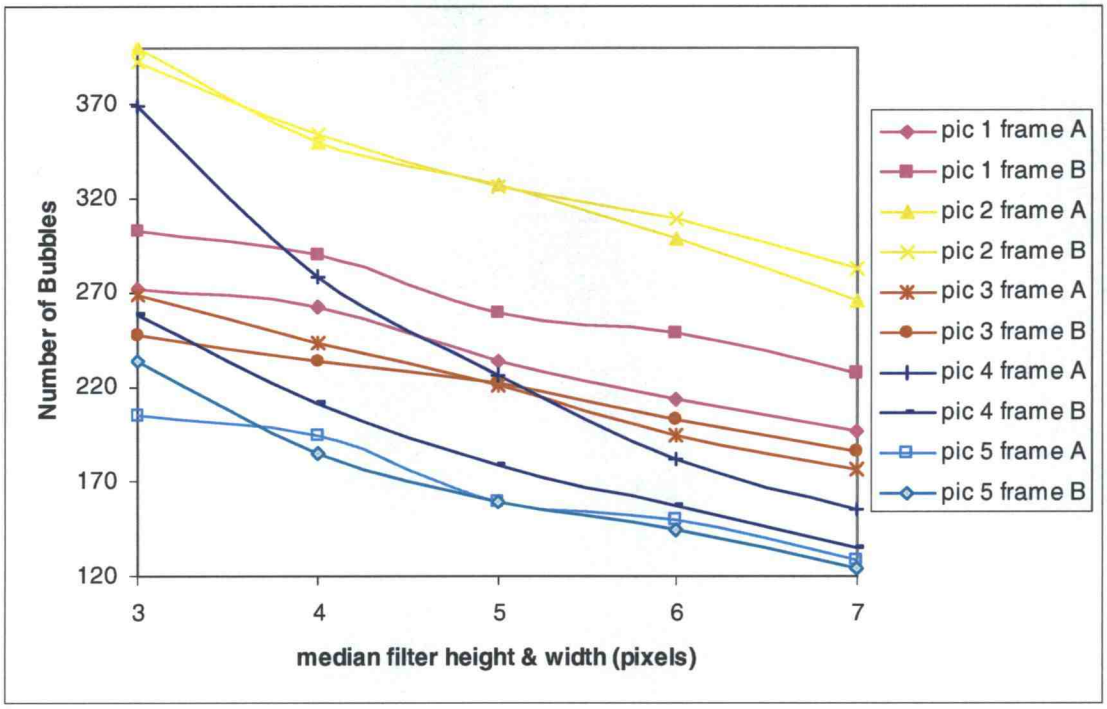

Figure 21. Sensitivity of number of bubbles to median filter size

Finally, the sensitivity of mean separation distance to filter size is displayed in Figures 22-24. While changing Disk 1 size has little effect, mean separation distance increases with increasing Disk 2 and median filter sizes. This may be explained by considering the effect these filters had on the number of bubbles in a frame. If there are less bubbles in a frame it makes sense that the distance between each should be larger presuming that they are evenly distributed. As was shown above, the number of bubbles in a frame decreases with both increasing Disk 2 and median filter size. Thus it is not surprising that mean separation distances increase with increases in both Disk 2 and median filter sizes.

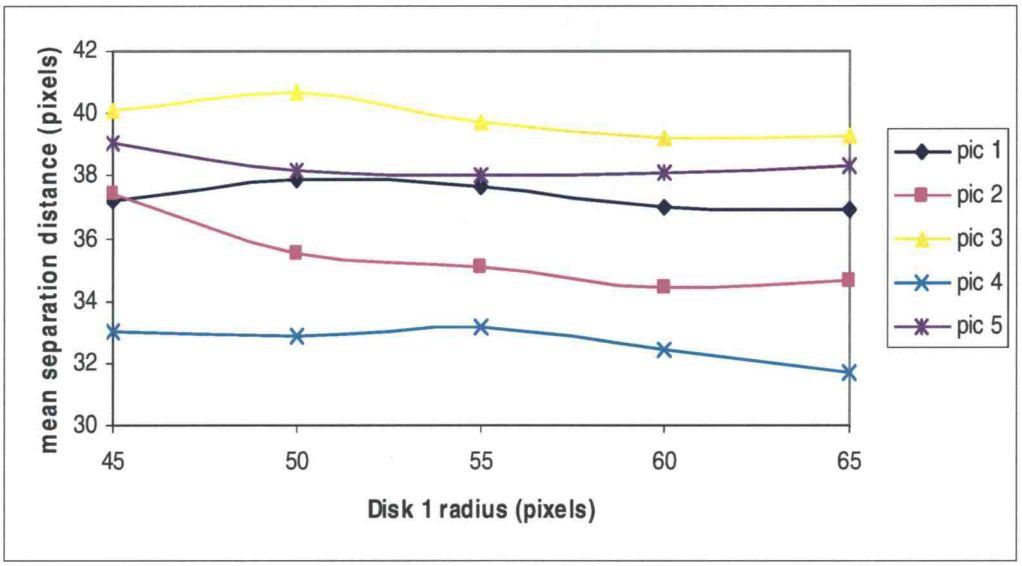

Figure 22. Sensitivity of mean separation distance to Disk 1 size

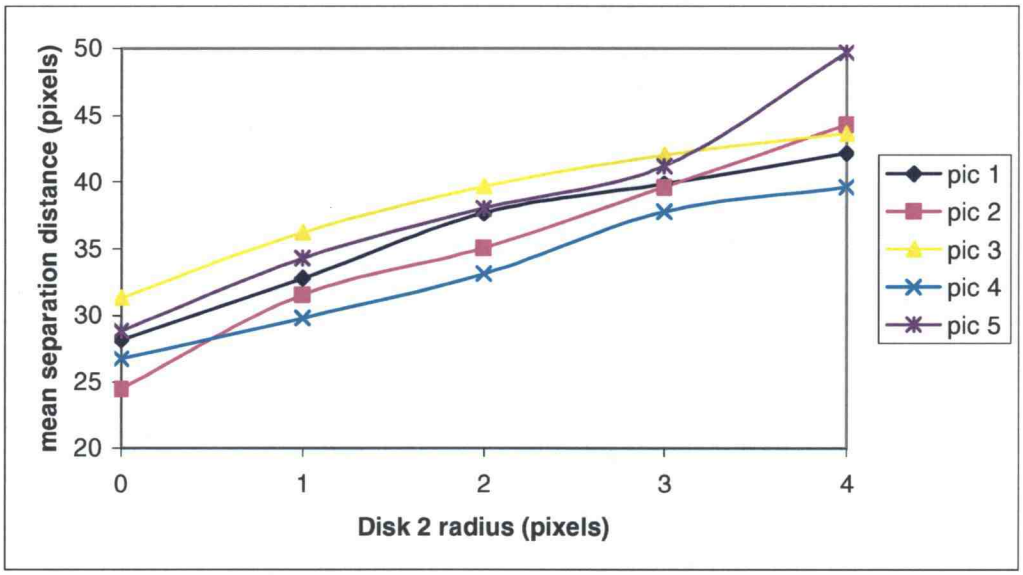

Figure 23. Sensitivity of mean separation distance to Disk 2 size

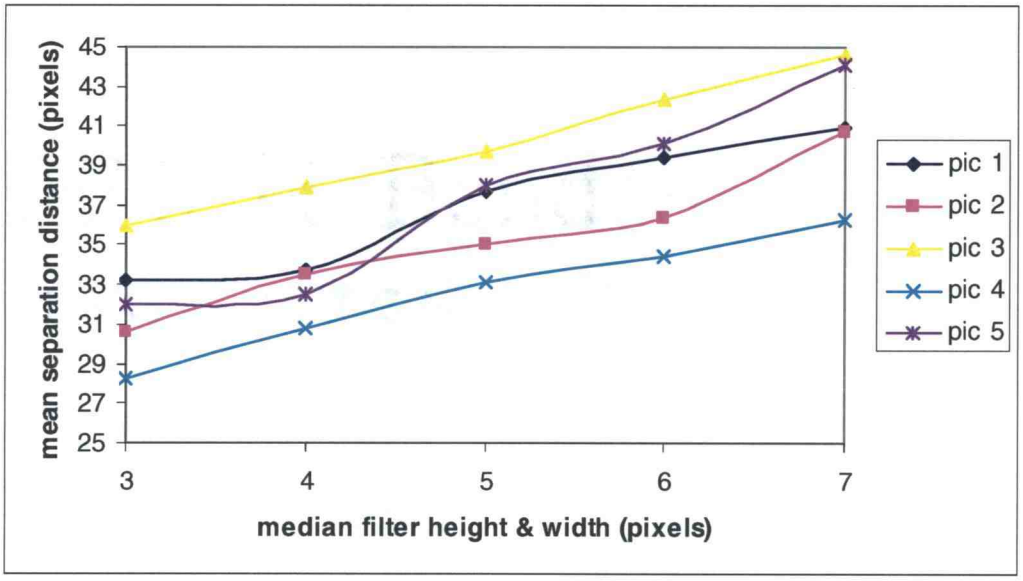

Figure 24. Sensitivity of mean separation distance to median filter size

Area fraction

Results for the area fraction are plotted in Figure 25. The average relative uncertainty in the area fraction was found to be ± 14.6% with the method described in Appendix C. From Figure 25 one can observe that increasing the applied electrolysis voltage did in fact increase area fractions. This effect is most easily seen in the data from y/h = 0.5. Comparing data points taken at the same flow rates one finds a larger area fraction for the higher voltage case. The results further indicate that area fraction reduced at higher flow rates. Inspection of the data for a flow rate of 40 mL/min shows area fractions typically near or above 0.06 while at 100 mL/min area fractions are consistently below 0.03. Additionally, examination of Figure 25 demonstrates that as the flow rate increases and electrolysis voltage remains the same, area fraction is reduced in all but one test. Recalling Faraday's law, it can be noted that the production rate of oxygen gas will remain roughly constant for the same electrolysis voltage. When flow rate doubles this same amount of gas is now dispersed in twice as much liquid, hence the area fraction should be approximately cut in half.

The results do not show the typical shape of void fraction distributions found in the literature (Kawamura 2004, Kitigawa 2005). Published results typically show that the void fraction increases with channel height to y/h ≈ 0.5-0.8 and then decreases. Although these experiments were done in larger channels with bubble injection from the upper channel wall one might expect a similar shape to profiles gained in the current study which uses bubbles generated at the lower channel wall. Disregarding results from experiments in larger channels, one may presume that area fraction distributions found at different conditions (flow rates, area fractions) in a micro-channel would be qualitatively similar to each other. Yet no consistent trends are apparent in the area fraction data. For example, the data for the 40 mL/min, 65 V test show an area fraction that decreases with height in the channel whereas at 40 mL/min and 90 Volts there is a peak in the area fraction distribution at y/h = 0.5. This clearly demonstrates that even at the same flow rate area fraction distributions fail to be reproduced qualitatively.

A few reasons for this may be considered. First, from monitoring channel flow visually during electrolysis and from processing hundreds of pictures it appears that electrolysis did not reliably create a homogenous spread of bubbles across the width of the channel. Rather, it seemed that at certain points along the electrolysis cathode bubbles were generated and carried downstream resulting in streaks of bubbles that stretched the length of the channel without significant mixing in the cross stream direction. Another affect which may play a role in the area fraction determination is depth of focus. While a depth of focus of 11 μm is calculated, it is possible that the optical set-up may have been unable to eliminate bubbles outside the field of measurement effectively. This effect would be most apparent at lower flow rates due to the higher area fractions and larger bubble diameters.

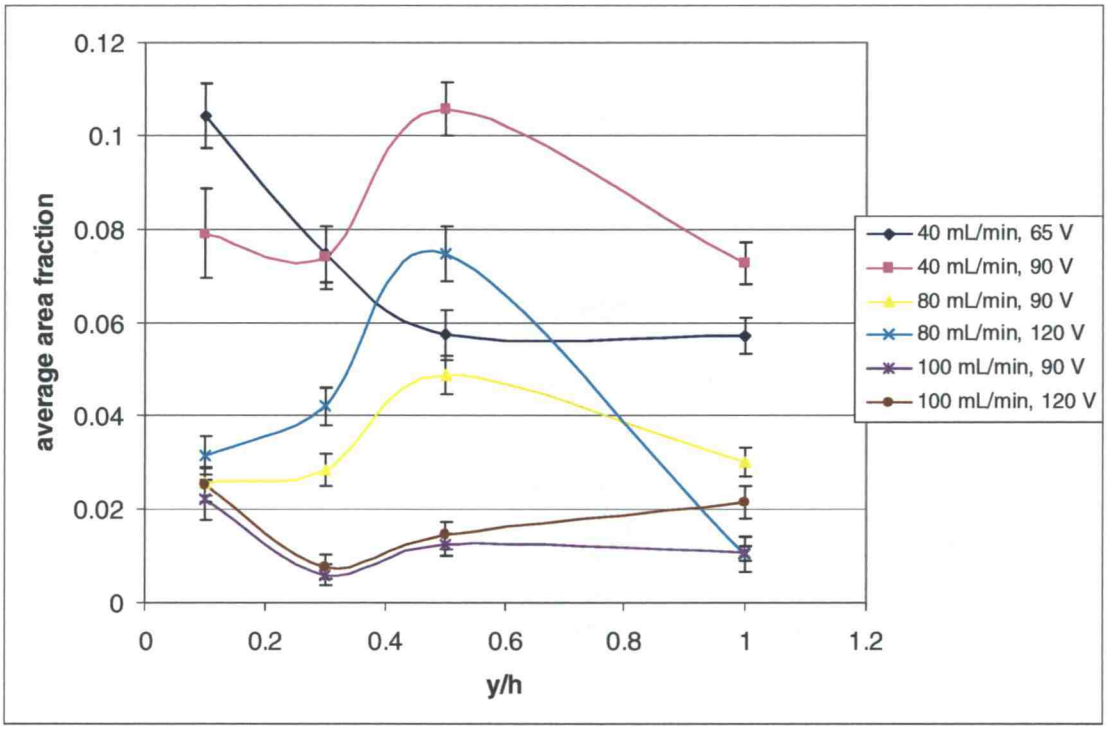

Figure 25. Area fraction results

Average bubble diameter

Results for average bubble diameters are plotted in Figure 26; the average relative uncertainty for bubble diameter data was ± 2% (Appendix C). From the literature it is shown that smaller bubbles disperse more quickly (Kawamura et al., 2004), yet this is not evident from the data in this study. For the low and middle flow rates one does find that the average bubble diameter is smaller in the middle of the channel than at y/h = 0.5, but this is not the case for the high flow rate. Figure 27 shows the relation of average bubble diameter to flow rate. Higher flow rates produce a larger shear at the electrolysis electrode with the consequence that gas has less time to congregate before being swept downstream. Thus, higher flow rates will generally produce small bubbles as Figure 27 demonstrates. The few data points that show an increased bubble diameter with flow rate are discussed in a following section.

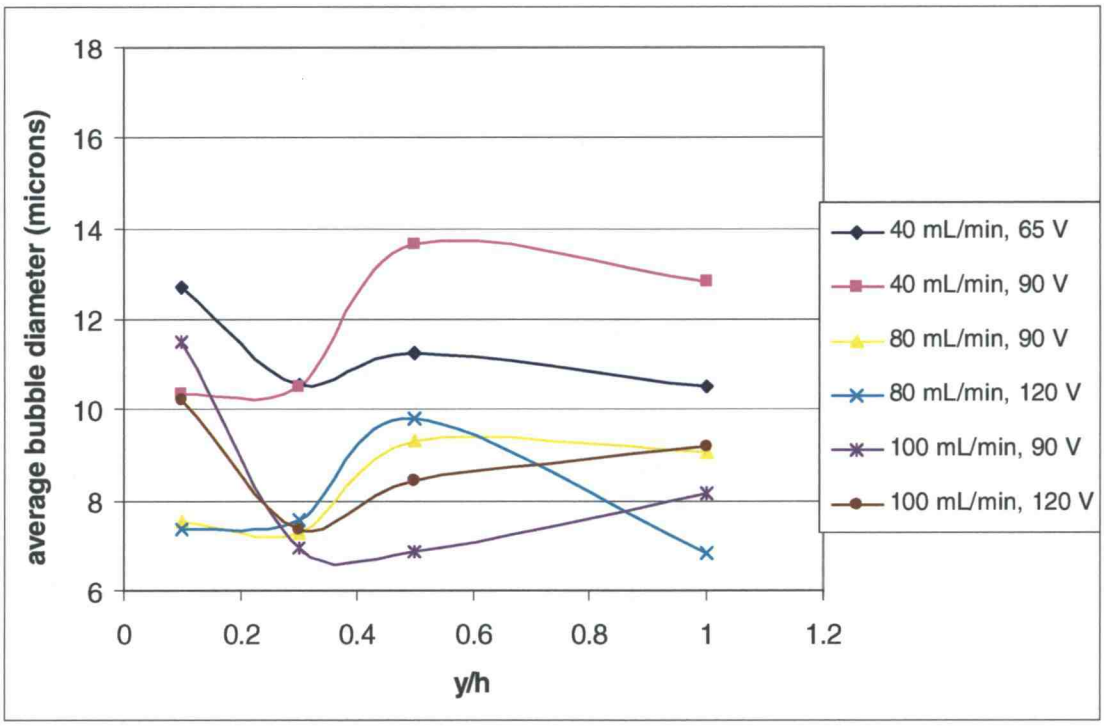

Figure 26. Average bubble diameter results

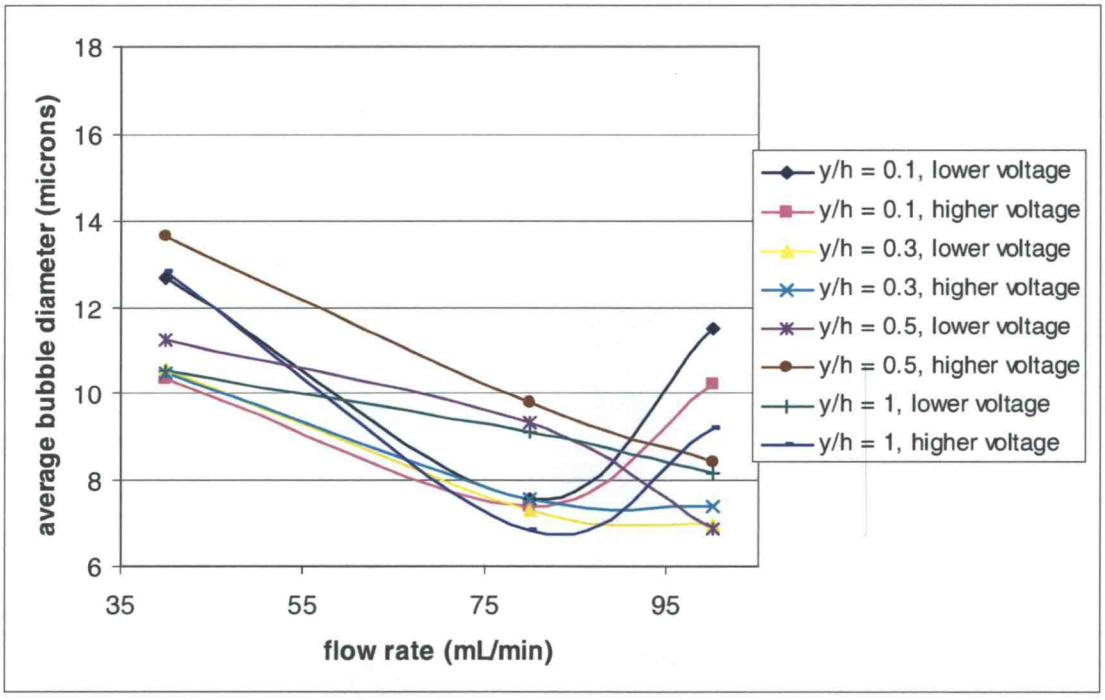

Figure 27. Average bubble diameter relation to flow rate

As a measure of how much noise is present, the average bubble diameter was calculated using only bubbles that were paired with the algorithm developed for bubble velocity determination. This algorithm, described in detail in Appendix B, pairs objects labeled in an eroded binary image pair based on restrictions of velocity, shape change, and placement in the frame. It is seen that when comparing average paired bubble diameter (Figure 28) and average bubble diameter (Figure 26) the plots are qualitatively similar but that the average paired bubble diameters are significantly larger. Figure 29 further illustrates how average paired bubble diameter results show the same trends as non-paired bubbles when compared with flow rate. Again, comparing Figures 27 and 29 it is found that the plots have similar shapes, though the average diameters are larger for paired bubbles. This increase in average diameter may indicate that noise is reduced through the pairing algorithm. As another check of this effect, a histogram of all bubble diameters and a histogram of paired bubble diameters from a single test condition are plotted (Figure 30). Examination of the histogram for all bubbles in a frame shows that the histogram has a peak around 1.5 μm, while the histogram for paired bubbles displays a peak around 8 μm. Noise is expected to typically be small in size and may include PIV tracer particles which are not removed during the digital image processing. Therefore it may be concluded that a limited amount of noise is paired compared to the amount of noise present in a given frame.

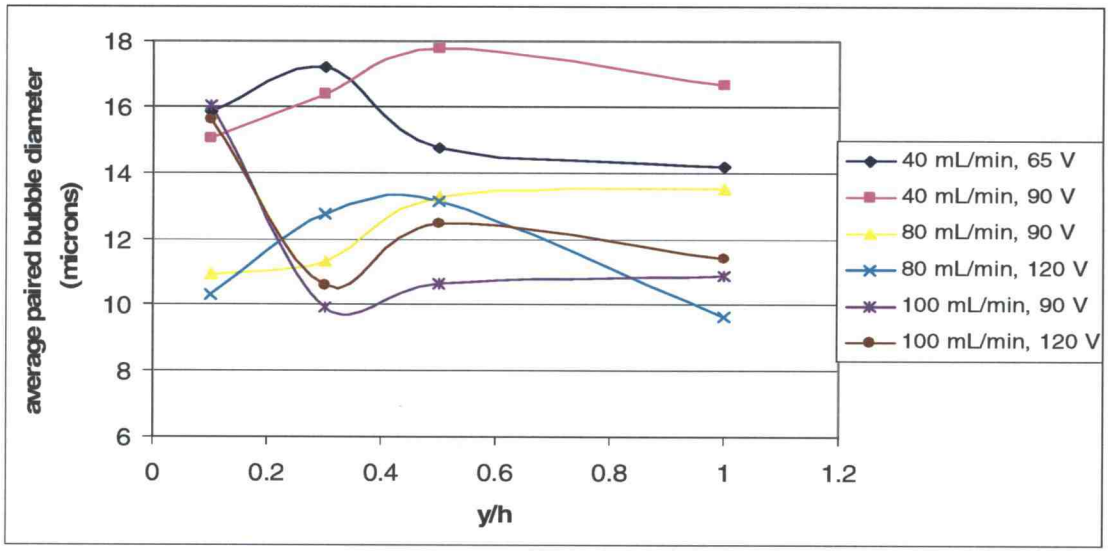

Figure 28. Average paired bubble diameter results

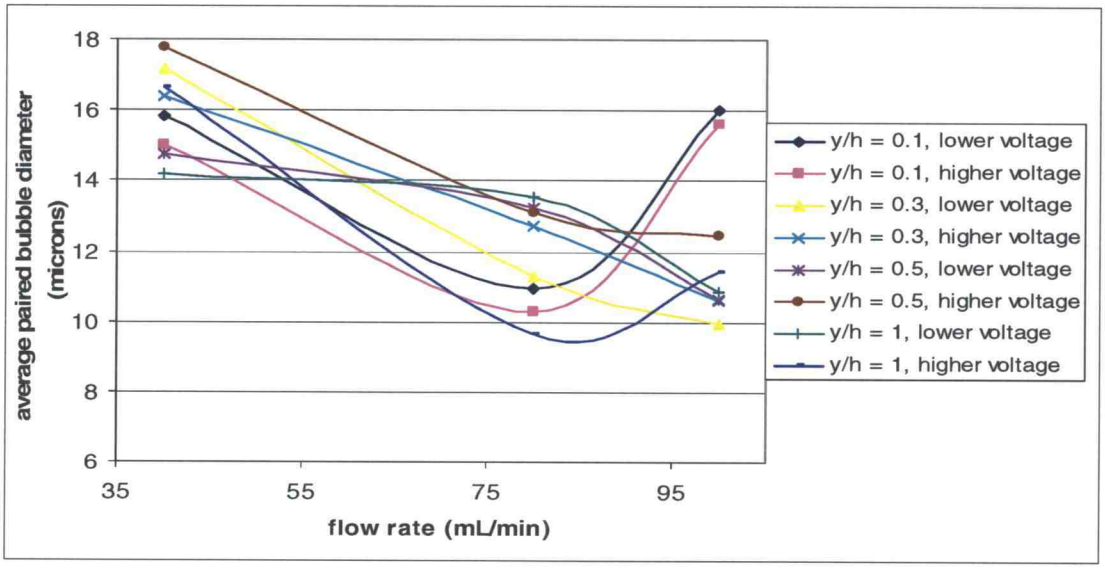

Figure 29. Average paired bubble diameter relation to flow rate

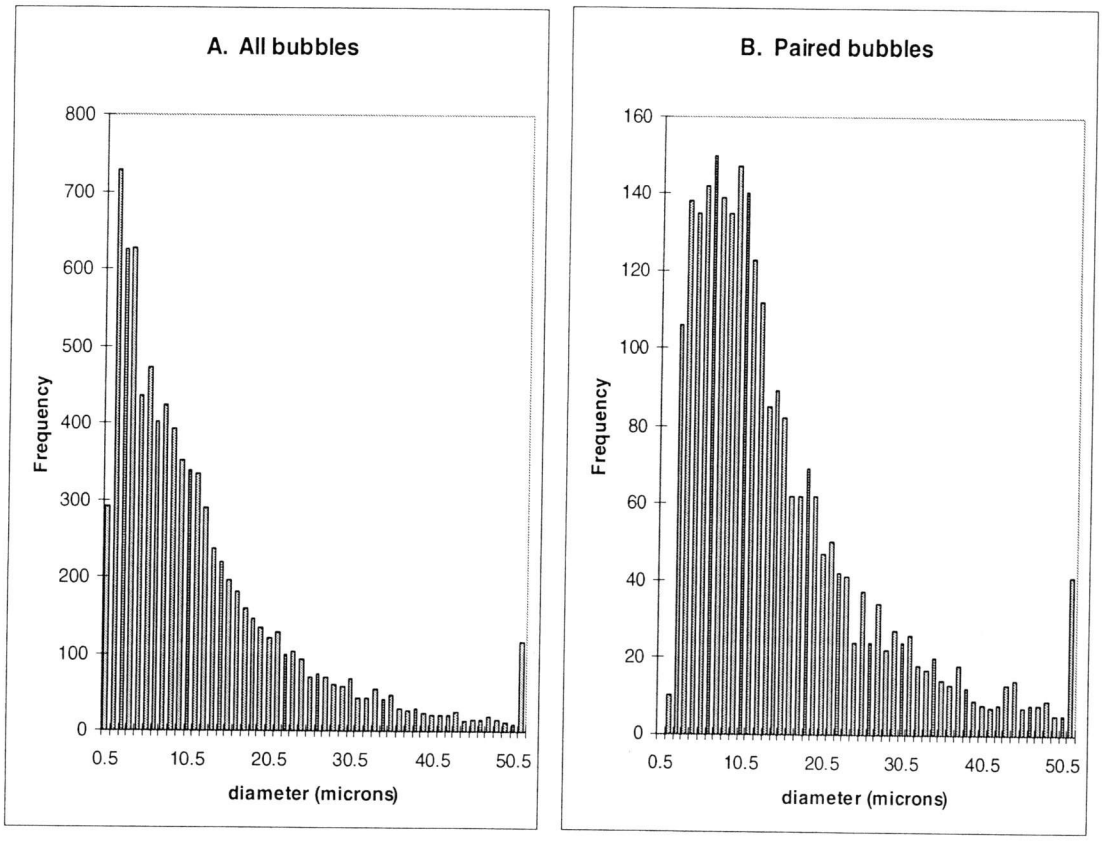

Figure 30. Histogram of all bubbles from a single test condition (A) and paired bubbles (B)

Average bubble velocity

Results for average bubble velocity are show in Figure 31. Also plotted are the theoretical values for fluid flow at the specified flow rates and channel heights. The theoretical curves vary from their expected parabolic shape due to slightly different channel heights measured for different tests (Table 2). Average velocity measurements had an average relative uncertainty of ± 3%. It is shown that measured average bubble velocities are typically larger than theoretical flow velocities at y/h = 0.1 and y/h = 0.3. This result is questionable and may be further evidence that bubbles higher in the channel are remaining in images taken at lower channel heights. Digital image processing effects from filtering/transforming an image may be raised as a possibility for this discrepancy, though there is little apparent reason why these

problems would be more prevalent in images taken lower in the channel than in images taken higher in the channel.

A further reason to question the validity of the process used for determining bubble velocity is found by scrutinizing how velocities change from y/h = 0.5 to y/h = 1. The data consistently show a drop in velocity occurring over this part of the channel. Assuming that the syringe pump is relatively consistent, this effect can only come from the optical set-up, image processing technique and/or the bubble pairing algorithm. For images taken at y/h = 1 it is expected that the number of bubbles higher in the channel than the plane of measurement would be less than for images taken at y/h = 0.5. Presuming that these bubbles remain in an image to some degree despite the limited focal depth of the optical set-up or image processing they can be considered a source of noise. Using this logic a case can be made that more noise is present in images from y/h = 0.5 than y/h = 1. With more noise present, it is easily imagined that more noise will be paired resulting in a less accurate average bubble velocity.

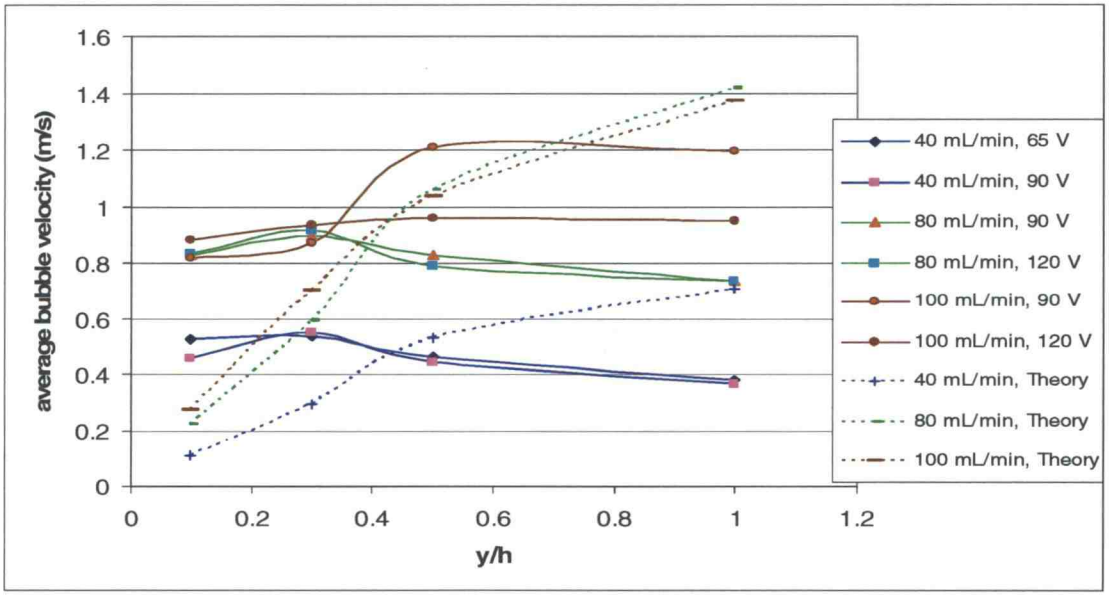

Figure 31. Average bubble velocity results

Finally, a velocity check was done with ten randomly selected images from different test conditions. In this check five bubbles were hand-picked from an image

pair following the digital image processing. These bubbles were chosen based on characteristics which would facilitate their recognition by MatLab and the bubble pairing algorithm: roughly round, same shape in each frame, away from edges of frame, etc. The velocities for these five bubbles were then averaged and compared to the original average bubble velocity determined for the image pair. Poor agreement was found between the average hand-picked bubble velocity and the total average bubble velocity (Table 4). Presumably, this difference is caused by noise that is paired. The nature of this noise is such that a judgment cannot be made as to which direction average velocity measurements will be biased.

Table 3. Relative average velocity difference found during velocity check

Pic. #	1	2	3	4	5	6	7	8	9	10
Relative velocity difference (%)	-18.2	-2.5	18.4	16.7	-4.0	-10.8	15.0	-3.9	20.4	-30.4

Figure 32 displays the relation of average bubble velocity to flow rate and gives further indication that velocity measurements are questionable. Presuming that bubbles will have a velocity similar to that of the flow, equation 4 indicates that data series in this plot should be linear. Yet most are not, and many of the trends show little to no increase in bubble velocity when flow rate is increased from 80 mL/min to 100 mL/min.

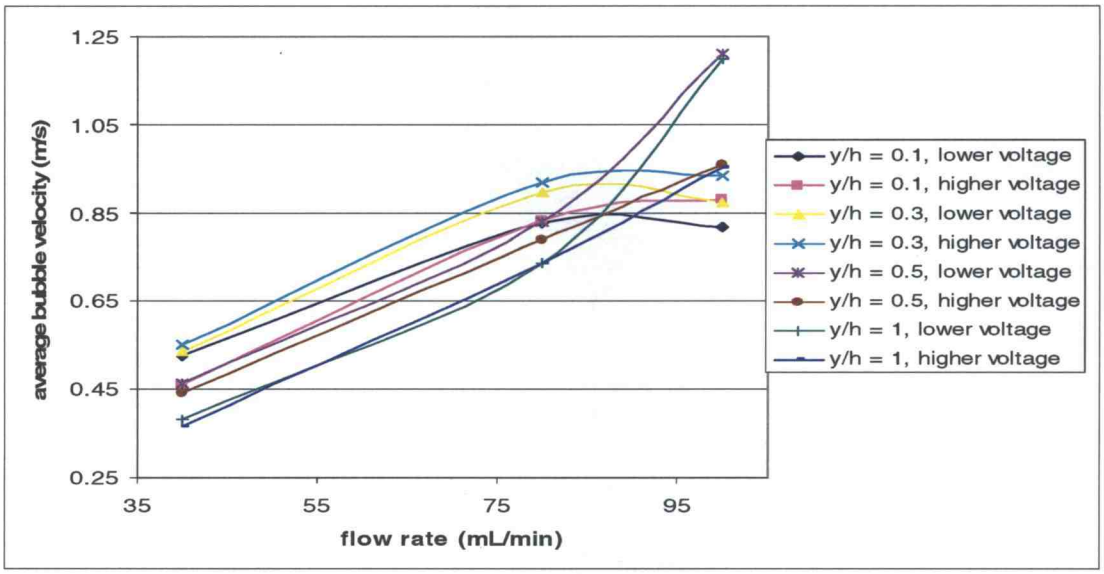

Figure 32. Average bubble velocity relation to flow rate

Correlations between flow rates

The use of electrolysis for bubble generation provided imprecise control of area fraction values, making it difficult to compare measurements taken at the same area fraction. Despite this fact, there are a few instances where similar area fractions were obtained. At y/h = 0.1 and for flow rates of 80 mL/min and 100 mL/min an average area fraction of ~ 0.02-0.03 was found. Comparison of data taken at these conditions can be made allowing conclusions on the effect of flow rate. As is shown in the Figures 33-35, when flow rate increases the average bubble diameter, average paired bubble diameter, mean separation distances, and mean separation distance standard deviations all increase. Even if bubbles higher in the channel are being captured it can be concluded that as flow rate increases bubbles uniformly spread out more and the standard deviation of this spread increases. If it can be shown that bubbles higher in the channel are not being captured one may conclude that for higher flow rates smaller bubbles disperse more quickly into the channel. This conclusion is based on the fact that as flow rate increases bubbles will be pulled off the electrolysis cathode more quickly and thus have a smaller diameter. Despite the reality that

bubble diameters are on average smaller we find a larger average bubble diameter at the y/h = 0.1 for the larger flow rate meaning that the smaller bubbles in the flow may have dispersed higher in the channel more quickly than the larger bubbles.

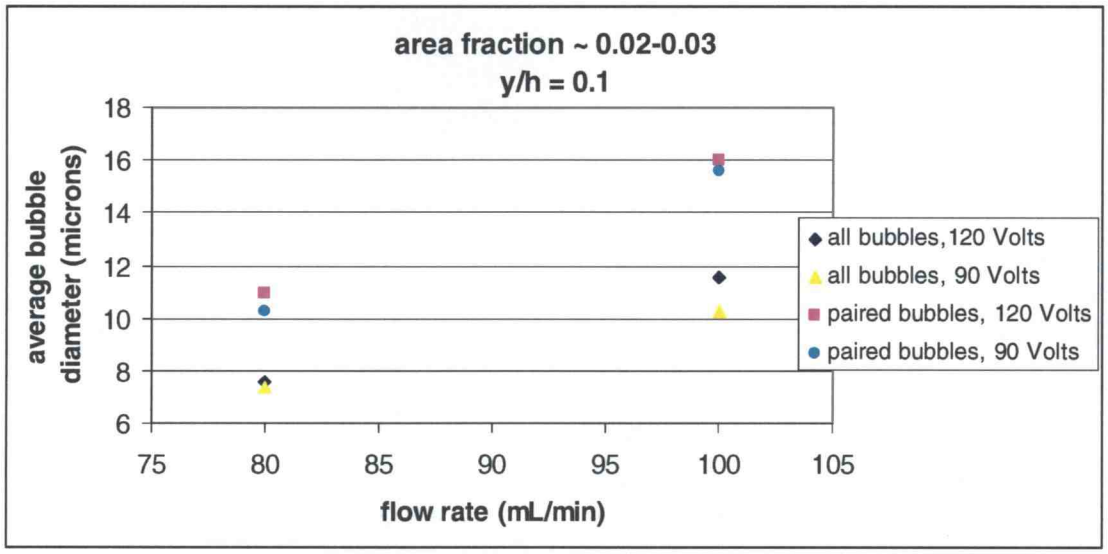

Figure 33. Comparison of average bubble diameters at different flow rates for area fraction ~ 0.02-0.03, y/h = 0.1

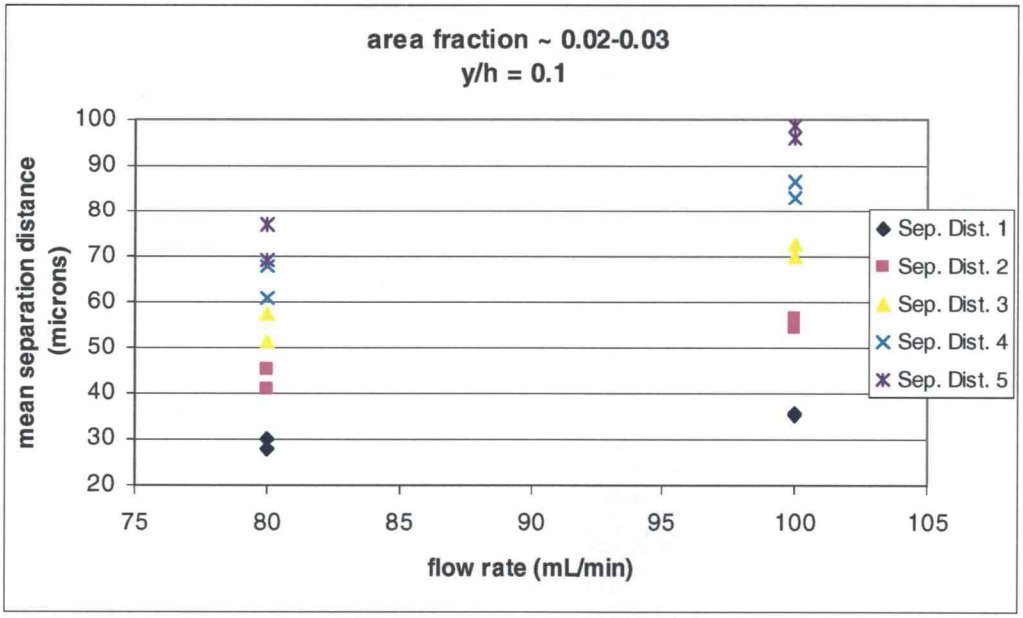

Figure 34. Comparison of mean separation distances at different flow rates for area fraction ~ 0.02-0.03, y/h = 0.1

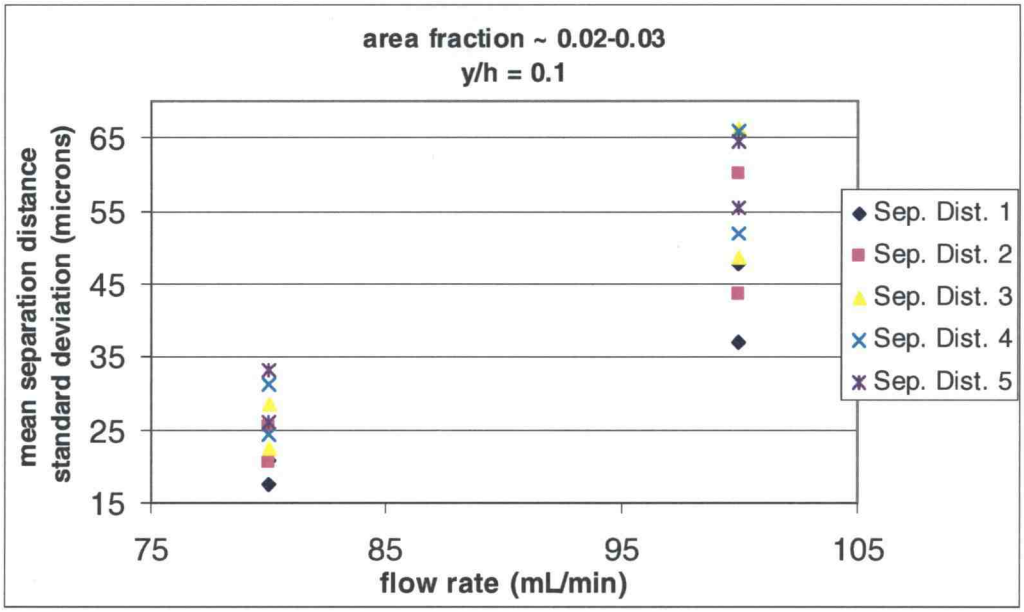

Figure 35. Comparison of mean separation distance standard deviations at different flow rates for area fraction ~ 0.02-0.03, y/h = 0.1

Another case of similar area fractions but different flow rates is found at y/h = 0.5 for flow rates of 80 mL/min and 100 mL/min with area fractions of ~ 0.01. The same trends are found for this example as in the previous in regards to the effect of increasing flow rate on average bubble diameter, average paired bubble diameter, mean separation distances, and mean separation distance standard deviations (Figures 36-38). Thus the same conclusions can be made and the case that smaller bubbles disperse more quickly can be made stronger. There is evidence that bubbles higher in the channel may cause increased noise and may even be captured in images where the focal plane is lower in the channel. This effect will be increased for lower flow rates and higher area fractions. Yet in the case under consideration here all of these effects are diminished because of the higher flow rates, smaller area fractions, and higher measurement position in the channel.

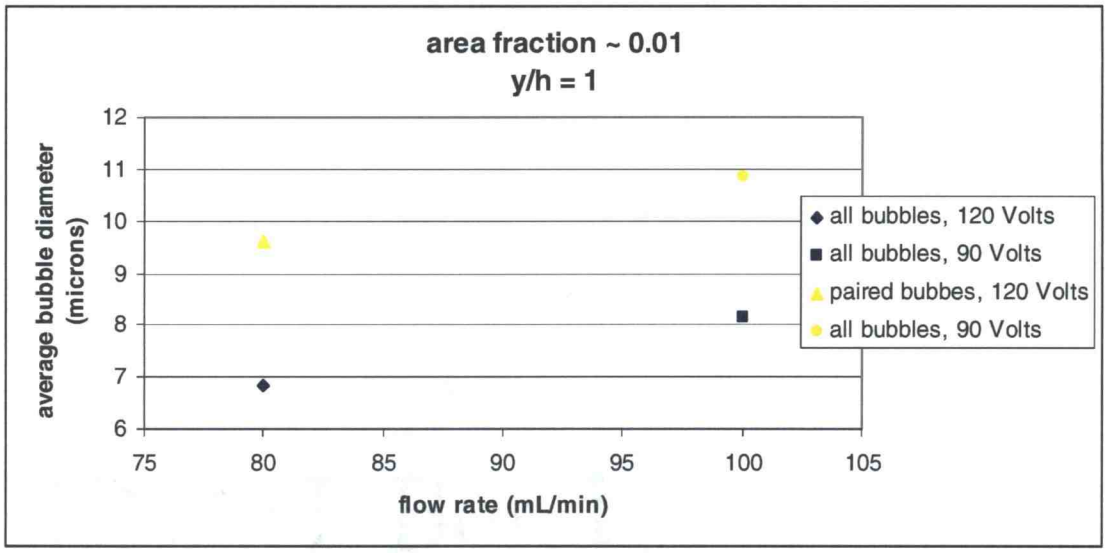

Figure 36. Comparison of average bubble diameters at different flow rates for area fraction ~ 0.01, y/h = 1

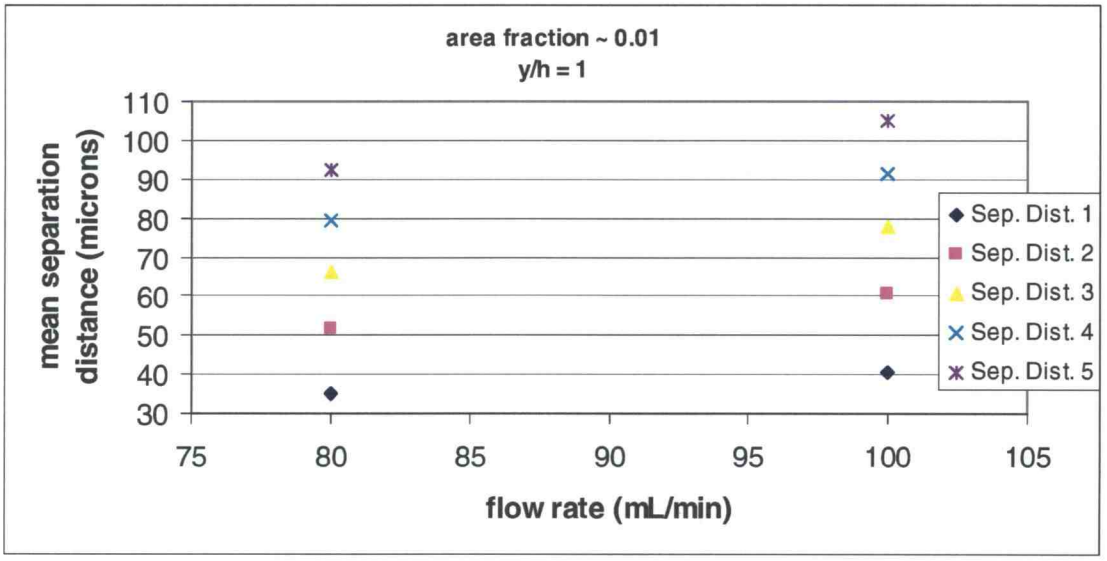

Figure 37. Comparison of mean separation distances at different flow rates for area fraction ~ 0.01, y/h = 1

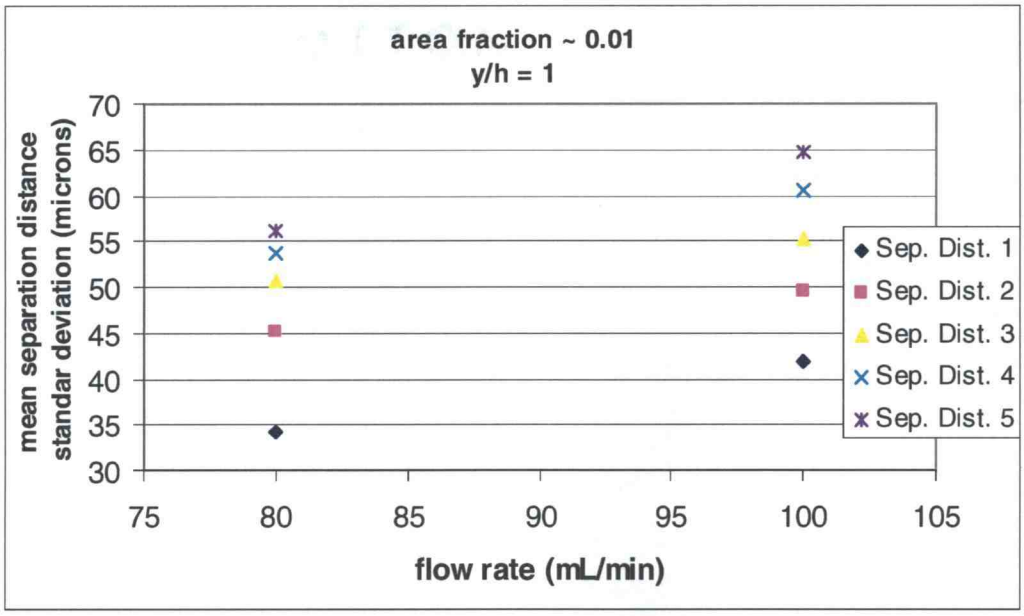

Figure 38. Comparison of mean separation distance standard deviations at different flow rates for area fraction ~ 0.01, y/h = 1

CONCLUSIONS AND RECOMMENDATIONS

In this study a flow visualization technique utilizing fluorescent dye and tracer particles was used to study two-phase flow in a micro-channel. The gas phase of the flow was introduced via electrolysis and the area fraction was roughly controlled by varying the electrolysis voltage. By varying the area fraction and flow rates and taking measurements at four different channel heights, information on bubble dynamics was obtained. A digital image processing technique was used to separate bubble information from each image, and a bubble pairing algorithm was employed to determine bubble velocities.

With this process, a few conclusions can be made on bubble dynamics in a micro-channel. By comparison of tests done at the same channel height and area fraction but different flow velocities it is determined that as flow rate increases bubble separation distances uniformly increase as well as the standard deviation of this separation. There is also evidence that higher flow rates may lead to smaller bubbles being dispersed into the channel more quickly than larger bubbles.

Furthermore, increasing electrolysis voltage was found to increase area fractions, while increasing flow rate decreased area fractions. Additionally, higher flow rates produced bubbles with smaller average diameters. The method of bubble generation is concluded to be less than optimal for a couple of reasons. First, it was capable of only minimal overall area fractions at higher flow rates for the maximum voltage produced by the set-up. Secondly, it is noted that the interaction of the flow with the electrolysis cathode created streaks of bubbles that would run the length of the channel rather than a homogenous spread of bubbles across the width of the channel. This problem may be partially alleviated by roughing the electrolysis electrodes thus creating more bubble nucleation sites.

It is concluded that a fair amount of noise, which is small in size and may include PIV tracer particles, survives the digital image processing method used. The bubble pairing algorithm is shown to reduce this noise. There is also evidence that the optical set-up may be incapable of completely excluding bubbles that exist between

the focal plane and camera objective. This effect is believed to be more prevalent for larger bubbles, typical of lower flow rates, and larger area fractions. Due to these effects, the accuracy of measured bubble velocities is concluded to be very questionable by comparison with theoretical flow velocities and a velocity check done with hand-picked bubbles from a sampling of images.

From the digital image processing sensitivity analysis it is determined that measured values can depend significantly on the convolution window sizes used. During filtering, a larger erosion element is expected eliminate more noise though using this alone will also affect the size and shape of larger bubbles. To reduce this effect, the erosion could be followed by a dilation element which could return the bubbles which survive the erosion to near their original size and shape. While this would put a lower limit on detectable bubble size, the gains in noise reduction may prove superior. As further discovered in the digital image processing sensitivity analysis, the use of a larger median filter and smaller tophat transformation convolution window may further reduce noise levels. The image processing may also benefit from a focus criterion. Much of the published literature using imaging techniques for bubble measurement verifies that focusing conditions, based on intensity gradients, are commonly used for bubble detection.

As a first step in improving the experimental set-up laser noise must be reduced. This may be accomplished with the use of a different laser, or perhaps by using a higher power setting with the original laser, which would presumably have an ameliorated beam, and attenuating the intensity with a filter. To avoid the intensity inconsistencies for illuminated bubbles, different laser angles into the channel may be explored. Another step towards reducing noise created during illumination would be to use an optical filter with a more severe wavelength cutoff. As the reflected light intensity from the bubbles remains high even after propagating through a long pass optical filter it is believed that a second filtering of the signal may remove more of the 532 nm light.

In addition, the evidence that the optical set-up may, to some degree, capture bubbles outside of the focal plane requires some attention. A test is needed to

determine the effectiveness of the set-up at eliminating bubbles outside of the desired measurement plane. One simple test could include the placement of larger (10-80 μm) microspheres into the channel. By viewing the channel from above and from below a determination of interference could be determined.

BIBLIOGRAPHY

Bröder, D., Sommerfeld, M., 2002, "Experimental studies of bubble interaction and coalescence in a turbulent flow by an imaging PIV/PTV system", *11th International Symposium on Applications of Laser Techniques to Fluid Mechanics*, Lisbon.

Cartellier, A., 2001, "Optical probes for multi-phase flow characterization: some recent improvements", *Chemical Engineering Technology*, Vol. 24, No. 5, pp. 535-538.

Cho, J., Perlin, M., Ceccio, S.L., 2005, "Measurement of near-wall stratified bubbly flows using electrical impedance", *Measurement Science Technology*, Vol. 16, pp. 1021-1029.

Deng, P., Lee, Y.K., Cheng, P., 2003, "The growth and collapse of a micro-bubble under pulse heating", *International Journal of Heat and Mass Transfer*, Vol. 46, No. 21, pp. 4041-4050.

Deutsch, S., Money, M., Fontaine, A., Petrie, H., 2003, "Microbubble drag reduction in rough walled turbulent boundary layers", *Proceedings of the 4th ASME/JSME joint fluids engineering conference and FED summer meeting and exposition CD-ROM*, Kauai, Hawaii, July 2003, paper no. FEDSM2003-45647, pp. 1-9.

Dinh, T.B., Kim, B.S., Choi, T.S., 1999, "Application of image processing techniques to air/water two-phase flow", *Proceedings of The International Society for Optical Engineering*, Vol. 3808, pp. 725-730.

Gui, L., Merzkirch, W., 1996, "Phase-separated PIV measurements in two-phase flow by applying a digital mask technique", *ERCOFTAC Bulletin*, Vol. 30, pp. 45-48.

Hepworth, N.J., Hammond, J.R.M., Varley, J., 2004, "Novel application of computer vision to determine bubble size distributions in beer", *Journal of Food Engineering*, Vol. 61, pp. 119-124.

Honkanen, M., Saarenrinne, P., 2002, "Turbulent bubbly flow measurements in a mixing vessel with PIV", *11th International Symposium on Applications of Laser Techniques to Fluid Mechanics*, Lisbon, Paper 3.2.

Kato, H., Iwashina, T., Migyana, M., et al., 1999, "Effect of microbubble clusters on turbulent flow structure", *IUTAM Symposium on Mechanics of Passive and Active Flow Control*, pp. 255-260.

Kawamura, T., Fujiwara, A., Takahashi, T., Kato, H., Matsumoto, Y., Kodama, Y., 2004, "The effects of the bubble size on the bubble dispersion and skin friction

reduction", *Proceedings of the 5th Symposium on Smart Control of Turbulence*, University of Tokyo, Tokyo, Japan, pp. 145-151.

Kevin, W., Skyba, D.M., Firschke, C., 1997, "Interactions between micro-bubbles and ultrasound: in vitro and in vivo observations", *Journal of the American College of Cardiology*, Vol. 29, No. 5, pp. 1081-1088.

Kitigawa, A., Fujiwara, A., Hishida, K., Kakugawa, A., Kodama, Y., 2003, "Turbulence structures of microbubble flow measured by PIV/PTV and LIF techniques", *Proceedings of the 3rd Symposium on Smart Control of Turbulence*, University of Tokyo, Tokyo, Japan, pp. 131-140.

Kitigawa, A., Hishida, K., Kodama, Y., 2005, "Flow structure of microbubbles-laden turbulent channel flow measured by PIV combined with the shadow image technique", *Experiments in Fluids*, Vol. 38, pp. 466-475.

Kodama, Y. Kakugawa, A., Takahashi, T., Nagaya, S., Sugiyama, K., 2002, "Microbubbles: drag reduction mechanism and applicability to ships", *Proceedings of the 24th symposium on naval hydrodynamics*, pp. 1-20.

Lee, S.J., Kim, S., 2005, "Simultaneous measurement of size and velocity of microbubbles moving in an opaque tube using X-ray particle tracking velocimetry technique", *Experiments in Fluids*, Vol. 39, pp. 490-495.

Lindken, R., Merzkirch, W., 1999, "Phase separated PIV and shadow-image measurements in bubbly two-phase flow", *Proceedings of the 8th International Conference on Laser Anemometry Advances and Applications*, Rome, Italy, pp. 165-171.

Lindken, R., Merzkirch, W., 2002, "A novel PIV technique for measurements in multi-phase flows and its application to two-phase flows", *Experiments in Fluids*, Vol. 33, No. 6, pp. 814-825.

Madavan, N.K., Deutsch, S., Merkle, C.L., 1984, "Reduction of turbulent skin friction by microbubbles", *Physics of Fluids*, Vol. 27, pp. 356-363.

Meinhart, C.D., Wereley, S.T., Santiago, J.G., 1999, "PIV measurements of a microchannel flow", *Experiments in Fluids*, Vol. 27, pp. 414-419.

Moriguchi, Y., Kato, H., 2002, "Influence of microbubble diameter and distribution on functional resistance reduction", *Journal of Marine Science Technology*, Vol. 7, pp. 79-85.

Sage, I., Humberstone, L., Oswald, I., Lloyd, P., Bourhill, G., 2001, "Getting light through black composites: embedded triboluminescent structural damage sensors", *Smart Materials and Structures*, Vol. 10, pp. 332-337.

Sridhar, G., Ran, B., Katz, J., 1991, "Implementation of particle image velocimetry to multi-phase flow", *Cavitation and Multiphase Flow Forum ASME-FED*, Vol. 109, pp. 205-210.

Wedin, R., Davoust, L., Cartellier, A., Byrne, P., 2003, "Experiments and modeling on electrochemically generated bubble flows", *Experimental Thermal and Fluid Science*, Vol. 27, pp. 685-696.

Xu, J., Maxey, M.R., Karniadakis, G.E., 2002, "Numerical simulation of turbulent drag reduction using micro-bubbles", *Journal of Fluid Mechanics*, Vol. 468, pp. 271-281.

APPENDICES

A: Threshold Determination

In a handful of instances images were removed from the data analysis and thrown out. The need for this relates to the varying noise levels which appeared in images. A few circumstances could not be reconciled effectively due to an unusual image illumination causing excessive noise as exemplified in Figure 39. In the process of determining an intensity threshold with which a filtered image could be turned binary the two major considerations were noise intensity and bubble interior intensity. Perhaps due to laser angle and reflective behaviors, the intensity of bubble circumference illumination was not constant for a given bubble. By this it is meant that while one part of the bubble's outer edge was very bright another part may have a much lower intensity. For this reason a bubble's interior would not always obtain an intensity significantly larger than that of the noise after the fill holes command. Yet, in order for that interior of that bubble to be binarized the threshold intensity had to be lower than the intensity of the bubble's interior.

Ideally there would be no noise and the entire background of a filtered image would be black allowing a very small threshold intensity to be chosen thus capturing all of the bubbles. Unfortunately noise was present in many pictures which remained after filtering. Before an image was turned binary the maximum noise intensity was also examined. Initially the intensity threshold would be chosen as the intensity of the maximum noise, but this would frequently lead to the interior of many bubbles being left out. At this point the iterative process for threshold determination began with the end result being a compromise between binarizing all bubble interiors and binarizing noise.

Figure 39. Example of excessive noise

A final criterion used when determining if a threshold was set correctly was continuity of bubble shape. As the image processing was done to both frames of an image pair it is desirable that a bubble in both frames retain its shape from the first frame to the second. Due to the aberrant noise behaviors this was occasionally not possible. A change in bubble shape due to noise patterns is detrimental inasmuch as the centroid of that bubble will be affected by the change in shape. This gives rise to a questionable bubble velocity. As a compromise was frequently made between detecting every bubble interior and removing noise during binarization it would not be uncommon for a handful of bubbles in a given frame to be detected with crescent shape. Noting this, an attempt would be made for a crescent shaped bubble in the first frame to remain crescent shaped in the second frame while at the same time limiting the amount of noise binarized. An example of crescent shaped bubbles and their continuity from the first frame to the second can be found by comparing Figures 40 and 41, paying close attention to the lower middle part of the image.

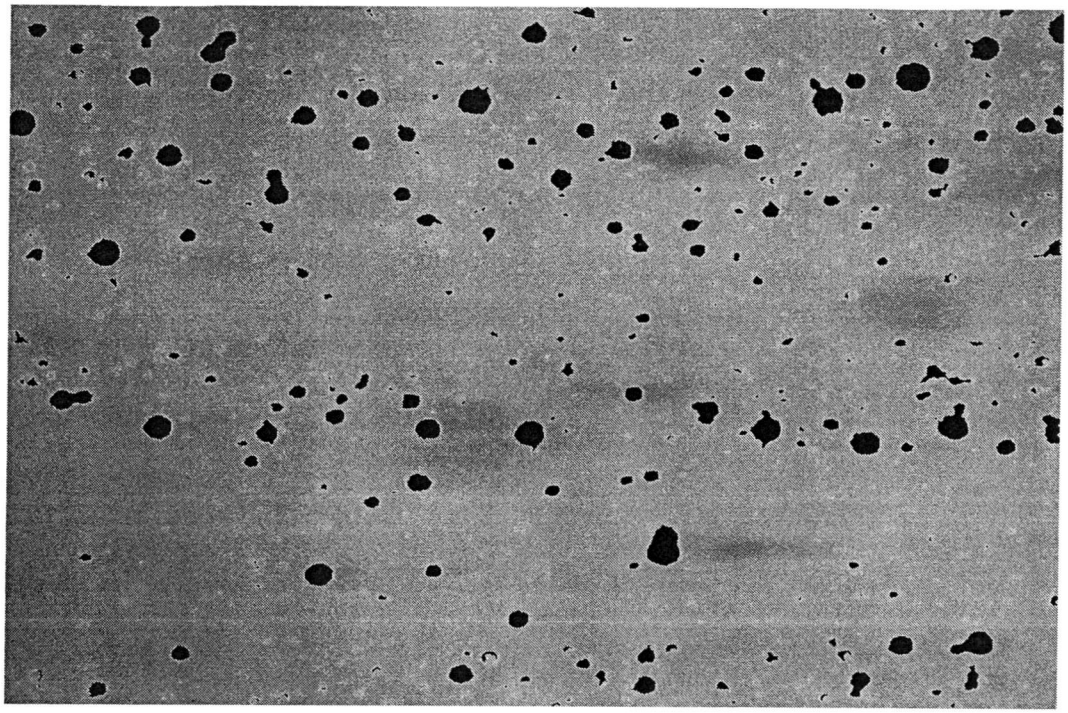

Figure 40. Frame A of image pair

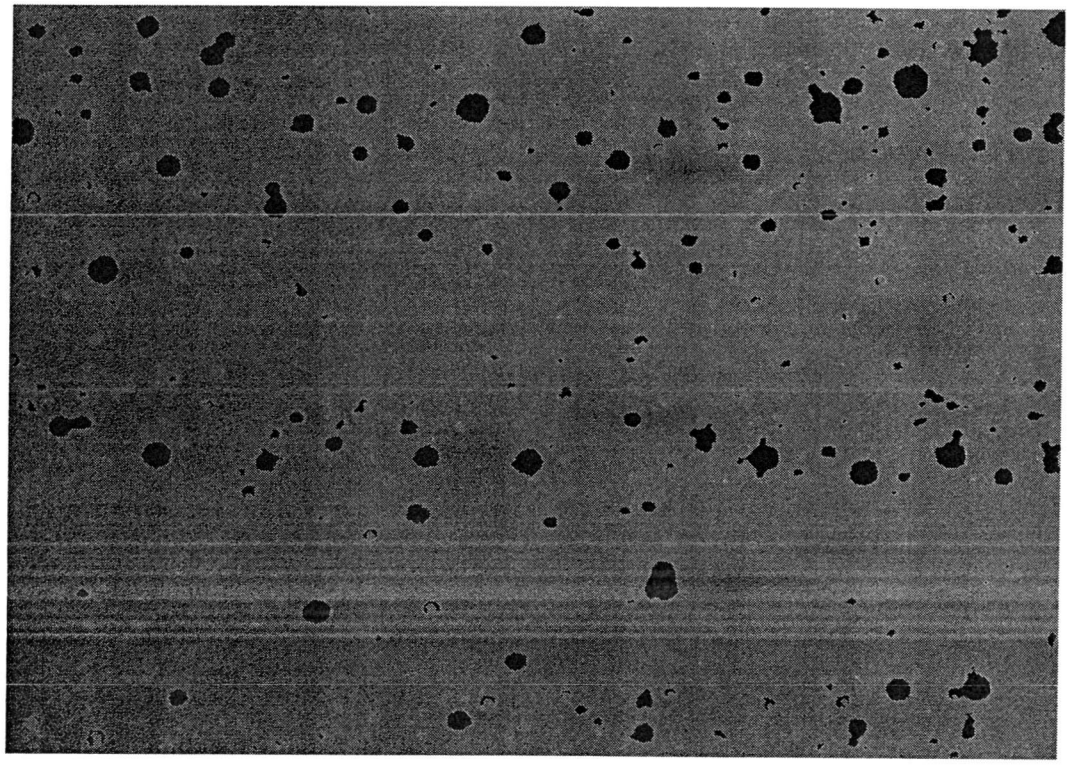

Figure 41. Frame B of image pair

B: Bubble Pairing/Velocity Algorithm

The algorithm developed to pair bubbles takes into account many factors. First, bubbles need to move in the direction of the flow. Second, a bubble's y-displacement must be less than 20% of its x-displacement. Third, a bubble's eccentricity may not change more than 20% from one frame to the next. This was included because bubbles overlapping in one frame would not necessarily overlap in the other frame. Overlapping bubbles would be considered as a single bubble, but if they were separate in the other frame their eccentricities would change. Fourth, the area of a picture in which present bubbles are available for comparison is limited. This is done so that bubbles that leave a frame or enter a frame do not get paired.

In order to determine the relevant cutoff distances with which to limit the frame area, a calculation of the rough average bubble displacement is done. In this calculation bubbles must move in the direction of flow and cannot have a displacement greater than 250 pixels. The latter criterion was required because it was discovered that for pictures with very few bubbles it occurred that bubbles very far apart could be paired leading to an unrealistically large average displacement. It should be noted that the choice of 250 pixels is many times larger than most average displacements. For each image pair a rough average x-displacement, y-displacement, and total displacement was calculated. Cutoff distances were determined as such:

x-cutoff = rough average x-displacement + 2 standard deviations

y-cutoff = rough average y-displacement + 2 standard deviations

d-cutoff = rough average total displacement + 2 standard deviations

The area of interrogation for which bubbles in the first frame could be paired was:

$$x\text{-cutoff} < x < 1300$$

$$y\text{-cutoff} < y < 1030 - y\text{-cutoff}$$

For the second frame the area was defined as:

$$0 < x < 1300 - x\text{-cutoff}$$

$$y\text{-cutoff} < y < 1030 - y\text{-cutoff}$$

Bubbles with centroids that were not in the area defined inside the cutoff distances, defined as the white areas in Figure 42, were not allowed to be paired. Additionally, bubbles with displacements above the d-cutoff were removed. The final criterion was that a bubble could only be paired once. In the situation that a bubble was paired with multiple bubbles in the other frame its partner was deemed as the bubble which would produce the smallest displacement for the pair.

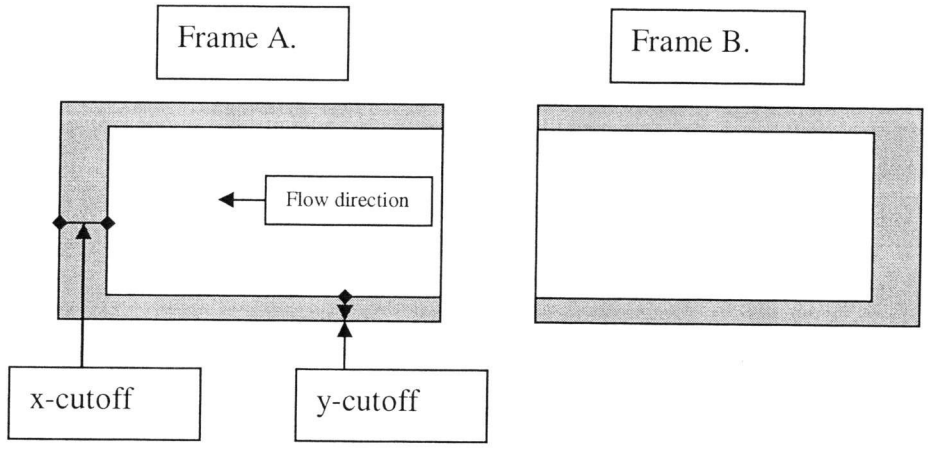

Figure 42. Areas of interrogation for bubble pairing

C: Uncertainty Analysis

Area fraction uncertainty

Finding area fraction precision error ($u_{a,p}$):

$$u_{a,p} = \pm t[0.025, n-1]\frac{std[AreaA;B]}{\sqrt{n-1}} \tag{7}$$

n = total number of frames in test

$[AreaA;B]$ = column of all area fractions from frames A and B of an image pair

Finding area fraction bias error ($u_{a,b}$):

- Make histogram of all bubbles in frames A and B with N bins of width = 1 μm
- Divide histogram by n
- Round numbers to nearest integer
- This provides average bubble diameter distribution for a frame

$$area\ fraction = \frac{\sum_{i=1}^{N} n_i \pi D_i^2}{4A_{total}} \tag{8}$$

n_i = number of bubbles in bin i

D_i = diameter of bubbles in bin i = $P_i C$

C = 0.81 μm/pixel

N = 160 bins

δ_p = ± 0.5 pixel

$$area\ fraction = \frac{\pi C^2}{4C^2 1030 * 1300}\sum_{i=1}^{N} n_i P_i^2 = \frac{\pi}{8034000}\sum_{i=1}^{N} n_i P_i^2 \tag{9}$$

$$u_{a,b} = \pm \frac{\pi}{4017000} \left(\sum_{i=1}^{N} (n_i P_i \delta_p)^2 \right)^{\frac{1}{2}} \quad (10)$$

$$u_{a,tot} = \pm \sqrt{u_{a,p}^2 + u_{a,b}^2} \quad (11)$$

Average bubble velocity uncertainty

- For each test an average displacement is found from the displacements of each paired bubble:

$$\overline{Disp} = \frac{1}{n_i} \sum_{i=1}^{n_i} Disp_i \quad (12)$$

i = specific bubble pair number (i.e. bubble pair 1, etc.)

n_i = number of paired bubbles in a test

- The average displacement will have a precision and bias error:

$$u_{\overline{Disp},p} = \pm t[0.025, n_i - 1] \frac{std[Disp_i]}{\sqrt{n_i - 1}} \quad (13)$$

$$u_{\overline{Disp},b} = \pm \frac{\left(\sum_{j=1}^{n_i} \left((C\delta_P)^2 + \left(P_{disp_j} \delta_c \right)^2 \right) \right)^{\frac{1}{2}}}{n_i} \quad (14)$$

$$u_{\overline{Disp},tot} = \pm \sqrt{u_{\overline{Disp},p}^2 + u_{\overline{Disp},b}^2} \quad (15)$$

$$\overline{Velocity} = \frac{\overline{Disp}}{T} \quad (16)$$

$$u_{\overline{Velocity}} = \pm\left(\left(\frac{u_{\overline{Disp}}}{T}\right)^2 + \left(\frac{\overline{Disp}\ \delta t}{T^2}\right)^2\right)^{\frac{1}{2}} \quad (17)$$

$\delta t = \pm 2$ ns

Average bubble diameter uncertainty

$$\overline{D} = \frac{1}{N}\sum_{i=1}^{N} D_i \quad (18)$$

N = total number of bubbles in all frames for a test

Finding precision error:

$$u_{\overline{D},p} = \pm t[0.025, N-1]\frac{std[D]}{\sqrt{N-1}} \quad (19)$$

D = column of all diameters from all frames in a run

Finding bias error:

$$u_{\overline{D},b} = \pm\frac{\left(\sum_{i=1}^{n_i}\left((C\delta_P)^2 + (P_i\delta_c)^2\right)\right)^{\frac{1}{2}}}{N} \quad (20)$$

$$u_{\overline{D},tot} = \pm\sqrt{u_{\overline{D},p}^2 + u_{\overline{D},b}^2} \quad (21)$$

Mean separation distance uncertainty

- To find the mean separation distance in a single frame (MSD_{avg}), the distance from a bubble's centroid to all other bubble centroids is determined and the minimum (msd) is recorded. This is repeated for every single bubble in the

frame giving a distribution of minimum separation distances. Thus for each frame a precision error and bias error can be calculated:

$$MSD_{avgi} = \frac{1}{n_i}\sum_{j=1}^{n_i} msd_j \tag{22}$$

i = specific frame number (i.e. frame 17, etc.)

j = specific bubble number in frame i

n_i = number of paired bubbles in frame i

- The average minimum separation distance will have a precision and bias error:

$$u_{MSD_{avgi},p} = \pm t[0.025, n_i - 1]\frac{std[msd_j]}{\sqrt{n_i - 1}} \tag{23}$$

$$u_{MSD_{avgi},b} = \pm\frac{\left(\sum_{j=1}^{n_i}\left((C\delta_P)^2 + \left(P_{msd_j}\delta_c\right)^2\right)\right)^{\frac{1}{2}}}{n_i} \tag{24}$$

$$u_{MSD_{avgi},tot} = \pm\sqrt{u^2_{MSD_{avgi},p} + u^2_{MSD_{avgi},b}} \tag{25}$$

- Having calculated the average minimum separation distance and its corresponding uncertainty allows the use of weighted averages to find the mean of the average minimum separation distances:

$$\overline{MSD} = \frac{\sum_{i=1}^{N} w_i MSD_{avgi}}{\sum_{i=1}^{N} w_i} \tag{26}$$

$$w_i = \frac{1}{u^2_{MSD_{avgi}tot}} \tag{27}$$

$$u_{\overline{MSD}} = \pm\left(\sum_{i=1}^{N} u_{MSD_{avgi}tot}^{2}\right)^{\frac{1}{2}} \tag{28}$$

N = number of image pairs

Table 4. Average relative uncertainties

	Relative Average Uncertainty (%)
Average Area Fraction	14.6
Average Bubble Diameter	2
Mean Separation Distance	1.6
Average Bubble Velocity	3